**WILEY**

# A coupled CFD-DEM investigation of suffusion of gap graded soil: Coupling effect of confining pressure and fines content

Yajing Liu[1,2]  |  Lizhong Wang[1,2]  |  Yi Hong[1,2] (ID)  |  Jidong Zhao[3] (ID)  |  Zhen-Yu Yin[4]

[1] Key Laboratory of Offshore Geotechnics and Material of Zhejiang Province, Hangzhou, China

[2] College of Civil Engineering and Architecture, Zhejiang University, Hangzhou, China

[3] Department of Civil and Environmental Engineering, The Hong Kong University of Science and Technology, Clear Water Bay, Kowloon, Hong Kong, China

[4] Department of Civil and Environmental Engineering, The Hong Kong Polytechnic University, Kowloon, Hong Kong, China

**Correspondence**
Yi Hong, Anzhong Building, Zijingang Campus, Zhejiang University, Hangzhou, China.
Email: yi_hong@zju.edu.cn

**Abstract**

Suffusion involves fine particles migration within the matrix of coarse fraction under seepage flow, which usually occurs in the gap-graded material of dams and levees. Key factors controlling the soil erodibility include confining pressure ($p'$) and fines content ($F_c$), of which the coupling effect on suffusion still remains contradictory, as concluded from different studies considering narrow scope of these factors. For this reason, a systematical numerical simulation that considers a relative wide range of $p'$ and $F_c$ was performed with the coupled discrete element method and computational fluid dynamics approach. Two distinct macroresponses of soil suffusion to $p'$ were revealed, ie, for a given hydraulic gradient $i = 2$, an increase in $p'$ intensifies the suffusion of soil with fines overfilling the voids (eg, $F_c = 35\%$), but have negligible effects on the suffusion of gap-graded soil containing fines underfilling the voids (eg, $F_c = 20\%$). The micromechanical analyses, including force chain buckling and strain energy release, reveal that when the fines overfilled the voids between coarse particles (eg, $F_c = 35\%$) and participated heavily in load-bearing, the erosion of fines under high $i$ could cause the collapse of the original force transmission structure. The release of higher strain energy within samples under higher $p'$ accelerated particle movement and intensified suffusion. Conversely, in the case where the fines underfilled the voids between coarse particles (eg, $F_c = 20\%$), the selective erosion of fines had little influence on the force network. High $p'$ in this case prevented suffusion.

**KEYWORDS**
CFD-DEM, confining pressure, fines content, force chain buckling, strain energy, suffusion

## 1 | INTRODUCTION

Suffusion usually occurs within gap-graded coarse material, where the instability and loss of fines are triggered under the action of seepage as shown in Figure 1A. It is indisputable that the significant changes of hydraulic and mechanical behavior of the soil induced by suffusion are the cause of many unfavorable evolutions, which may lead to failure. Previous experimental and theoretical studies on suffusion have revealed that the erodibility of gap-graded soil is significantly influenced by confining pressure ($p'$) and fines content ($F_c$).[1–14] It was concluded from some studies that a higher confining
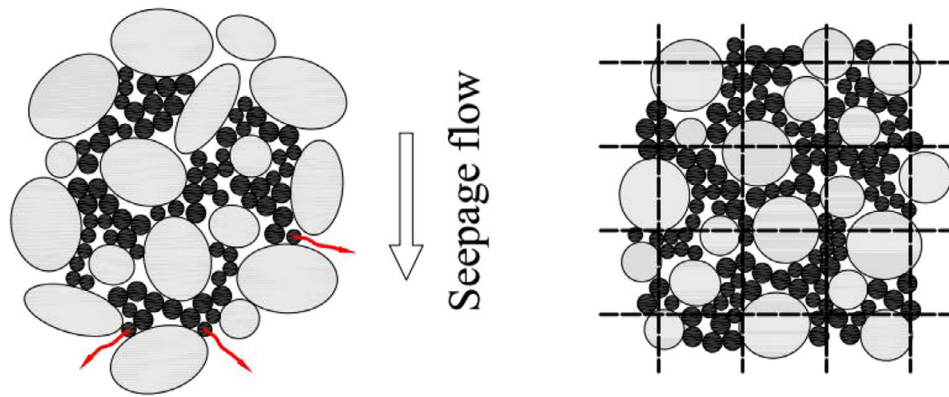
**FIGURE 1** (A) Illustration of internal erosion and (B) schematic diagram of coarse grid DEM-CFD simulation approach adopted in this study

pressure ($p'$) may help to prevent the occurrence of suffusion, due to the resulted increase in the interparticle contact force and particle connectivity.[8,9,15,16] Conversely, it was revealed from other studies that an increasing confining pressure could have intensified the suffusion (e.g., more fines loss) of a gap-graded soil.[1-3,5,60] The contradictory observations on the influences of $p'$ probably are resulted from the narrow scope of the influential factors (ie, $p'$ and $F_c$) considered in each study. For example, most experiments revealing that suppressed erodability by higher $p'$ was generally carried out based on gap-graded soil with relatively low $F_c$ (fines underfilling the voids of coarse grains).[11,12] The tests showing intensified erodibility by higher $p'$ were mainly performed based on gap-graded soil with relatively high $F_c$ (fines overfilling the voids of coarse grains).[2,3,5,60]

Currently, numerical experiments of such problems were mainly carried out by the coupled computational fluid dynamics (CFD) and discrete element method (DEM) technique. Researchers utilized a coarse-grid CFD-DEM, in which a fluid grid accommodates about 10 particles as shown in Figure 1B, to investigate the microscopic particle erosion and transport process within gap-graded soils.[15–17] Some researchers adopted a fine-grid CFD-DEM, where the fluid grid is much smaller than a particle and their interactions are directly computed by the commonly used immersed boundary method, to study fluid particle systems.[18] Recently, a coupled lattice Boltzmann method (LBM), which is an advanced high-resolution CFD solver for fluid flow and DEM approach, has been attracting substantial attention of researchers in geomechanics. Its application in the erosion and subsequent migration of fine particles was first reported by Wang et al[19] An advanced algorithm of LBM-DEM can be found in the literature.[20]

In view of the aforementioned issues, this study aims to obtain a better understanding on the coupling effect of $F_c$ and $p'$ on the erodibility of gap-graded sand samples, and to shed micromechanical insights into the phenomenon. Given the computational power and efficiency of current computers, this is achieved by performing coupled DEM and CFD simulations on the suffusion of gap-graded sand samples, with consideration of a broad range of $F_c$ and $p'$, using the coarse-grid CFD-DEM technique. The simulated macroresponse (including the eroded particles mass and samples deformation) were presented, showing distinct roles played by $p'$ at different $F_c$, ie, suppressed erodibility by increasing $p'$ at relatively low $F_c$, and intensified erodibility by increasing $p'$ at relatively higher $F_c$. These distinct responses are interpreted from the micromechanical perspectives, including evolving of loading bearing, force chain buckling, and strain energy. The shear stress ($q$) and soil density are not considered in this study. Both of them also have significant effects on suffusion,[7,21–23] which could be analyzed in future work.

## 2 | COUPLED CFD-DEM METHOD

The coupled CFD-DEM method used in this study included three types of formulations: the DEM, CFD, and the CFD-DEM coupling formulation. The DEM code LIGGGHTS is responsible for simulating massive dispersed particle bodies through Newton's law. The CFD code OpenFOAM is a common tool for simulating hydrodynamic processes through solving the continuity and Navier-Stokes equations. In this study, the particle-fluid interaction, including the drag force, pressure gradient force, and viscous force, is calculated by the CFDEM program developed by Goniva et al[24] and Kloss et al.[25] Governing equations for DEM, CFD, and coupling procedures are given in the following subsections.

## 2.1 | Governing equations for DEM

DEM is a widely used approach for simulating the behavior of massive dispersed particles based on Newton's second law of motion. At any time $t$, the equation governing the translational and rotational motion of particle $i$ is

$$
\begin{cases}
m_i \dfrac{d\mathbf{U}_i}{dt} = \displaystyle\sum_{j=1}^{n_i^c} \mathbf{F}_{ij}^c + \mathbf{F}_i^f \\
I_i \dfrac{d\boldsymbol{\omega}_i}{dt} = \displaystyle\sum_{j=1}^{n_i^c} \mathbf{M}_{ij}
\end{cases}, \tag{1}
$$

where $m_i$ and $I_i$ denote the mass and moment of inertia of particle $i$, respectively. $\mathbf{U}_i$ and $\boldsymbol{\omega}_i$ are the transitional and angular velocities of particle $i$, respectively. The forces involved include the contact force and torque acting on particle $i$ by particle $j$ (ie, $\mathbf{F}_{ij}^c$ and $\mathbf{M}_{ij}$), as well as the particle-fluid interaction force acting on particle $i$ (ie, $\mathbf{F}_i^f$). $n_i^c$ is the number of contacts of the particle $i$. In DEM code, and the Hertzian contact law[26,27] is employed in conjunction with Coulomb's friction law to describe the interparticle contact behavior. The contact behavior is governed by the normal and tangential stiffness at the contacts (ie, $k_t$ and $k_n$, respectively), as formulated below:

$$
k_n = \frac{4}{3} E^* \sqrt{R^* \delta_n}, \tag{2a}
$$

$$
k_t = 8 G^* \sqrt{R^* \delta_n}, \tag{2b}
$$

where $E^*$ and $G^*$ are the equivalent elastic and shear modulus, respectively. $R^*$ is the equivalent radius for two contacting particles. As shown in Equations 2(a) and (2b), both of the contact normal and tangential stiffness are functions of elastic moduli ($E^*$ and $G^*$), a particle-radius related parameter ($R^*$), and interparticle overlap ($\delta_n$). The term $E^*$, $G^*$, and $R^*$ can be further expressed as:

$$
\frac{1}{E^*} = \frac{1 - v_i^2}{E_i} + \frac{1 - v_j^2}{E_j}, \tag{3a}
$$

$$
\frac{1}{G^*} = \frac{2(2 + v_i)(1 - v_i)}{E_i} + \frac{2(2 + v_j)(1 - v_j)}{E_j}, \tag{3b}
$$

$$
\frac{1}{R^*} = \frac{1}{r_i} + \frac{1}{r_j}, \tag{3c}
$$

where $E_i$ and $Ej$ are the elastic moduli of two contacting particles $i$ and $j$; $v_i$ and $v_j$ are the Poisson's ratios of the particles $i$ and $j$; and $r_i$ and $r_j$ are the radii of the particles $i$ and $j$. It is worth noting that the elastic modulus and Poisson's ratio are material constants, while the particle radius and interparticle overlap ($\delta_n$) are variables being incrementally updated through the interactive process of DEM simulation. In this study, it is assumed that the elastic modulus and Poisson's ratio of each particle are identical (ie, $E_i = E_j$, $v_i = v_j$). The values of the material parameters, eg, elastic modulus and Poisson ratio are given in detail in Section 4.2.

## 2.2 | Governing equations for computational fluid dynamics

The CFD method solves the following continuity equation and locally averaged Navier-Stokes equation accounting for the presence of particles in the fluid.

$$
\begin{cases}
\dfrac{\partial(n\rho_f)}{\partial t} + \nabla \cdot (n\rho_f \mathbf{U}^f) = 0 \\
\dfrac{\partial(n\rho_f)}{\partial t} + \nabla \cdot (n\rho_f \mathbf{U}^f \mathbf{U}^f) - n\nabla \cdot (\mu\nabla\mathbf{U}^f) = -\nabla p - \mathbf{f}^p
\end{cases}, \tag{4}
$$

where $\mathbf{U}^f$ and $p$ are the average velocity and pressure of a fluid cell, respectively. $n$ is the local porosity that is used to account for the particle influence on the fluid computation. $\rho_f$ is the fluid density. The particle-fluid interaction force ($\mathbf{F}_i^f$) in Equation (1) is the fluid force acting on a single particle. The average particle-fluid interaction force ($\mathbf{f}^p$) in Equation (4) is the reaction force of the $\mathbf{F}_i^f$ within the volume of a fluid cell. The fluid force $\mathbf{f}^p$ is calculated as the summation of the fluid force acting on the particles in each fluid cell over the volume of the cell, ie, $\mathbf{f}^p = \sum_{i=1}^{k} \mathbf{F}_i^f / \Delta V$, where $\Delta V$ and $k$ denote the volume of a CFD cell and number of particles in the cell, respectively. $\rho$ and $\mu$ are the fluid density and viscosity, respectively. Numerically, the discretized cells are used to represent the continuous fluid domain. In each cell, variables such as density, fluid velocity, and pressure are locally averaged quantities.

## 2.3 | Governing equations for particle-fluid interaction forces

Previous research has shown that typical particle-fluid interaction forces include the drag force, pressure gradient force, buoyance force, and viscous force, as well as other unsteady forces such as virtual mass force, Basset force, and lift forces.[28] In a suffusion problem, the drag force, pressure gradient force, and viscous force are usually considered significant.(Hu et al, 2018),[65] Equation (5) shows the particle-fluid interaction forces ($\mathbf{F}^f$) considered in this study including drag force ($\mathbf{F}^d$), pressure gradient force ($\mathbf{F}^p$), and viscous force ($\mathbf{F}^v$), as shown below:

$$\mathbf{F}^f = \mathbf{F}^d + \mathbf{F}^p + \mathbf{F}^v. \tag{5}$$

The drag force is adopted from the expression proposed by Di Felice,[30] which is applicable for a dense granular regime and valid for a wide range of Reynolds numbers:

$$\begin{cases} \mathbf{F}^d = \dfrac{1}{8} C_d \rho_f \pi d_p^2 (\mathbf{U}^f - \mathbf{U}^p) \left| \mathbf{U}^f - \mathbf{U}^p \right| n^{1-\chi} \\[2ex] C_d = \left( 0.63 + \dfrac{4.8}{\sqrt{\mathrm{Re}_p}} \right)^2 \\[2ex] \mathrm{Re}_p = \dfrac{n \rho_f d_p \left| \mathbf{U}^f - \mathbf{U}^p \right|}{\mu} \\[2ex] \chi = 3.7 - 0.65 \exp \left[ -\dfrac{(1.5 - \log_{10} \mathrm{Re}_p)^2}{2} \right] \end{cases}, \tag{6}$$

where $d_p$ is the diameter of particles and $C_d$ is the particle-fluid drag coefficient for a single spherical particle that depends on the Reynolds number of the particle ($\mathrm{Re}_p$). $\chi$ in Equation (6) is a correlation function that modifies the coefficient of drag force accounting for the presence of other particles in the system.

The pressure gradient force ($\mathbf{F}^p$) and viscous force ($\mathbf{F}^v$) for a single particle are formulated by Equations (7) and (8), respectively[31]:

$$\mathbf{F}^p = -V_p \nabla p, \tag{7}$$

$$\mathbf{F}^v = V_p \nabla \cdot \tau, \tag{8}$$

where $V_p$ is the volume of the particle. $\tau$ is the viscous stress tensor that describes the friction between the fluid and the surface of particles.

## 3 | VALIDATION OF COUPLED CFD-DEM METHOD

This section aims to verify the coupled CFD-DEM method in the context of fluid-particle interaction (based on the locally averaged Navier-Stokes equation[32]), which governs suffusion. The predictive capability of the method for simulating
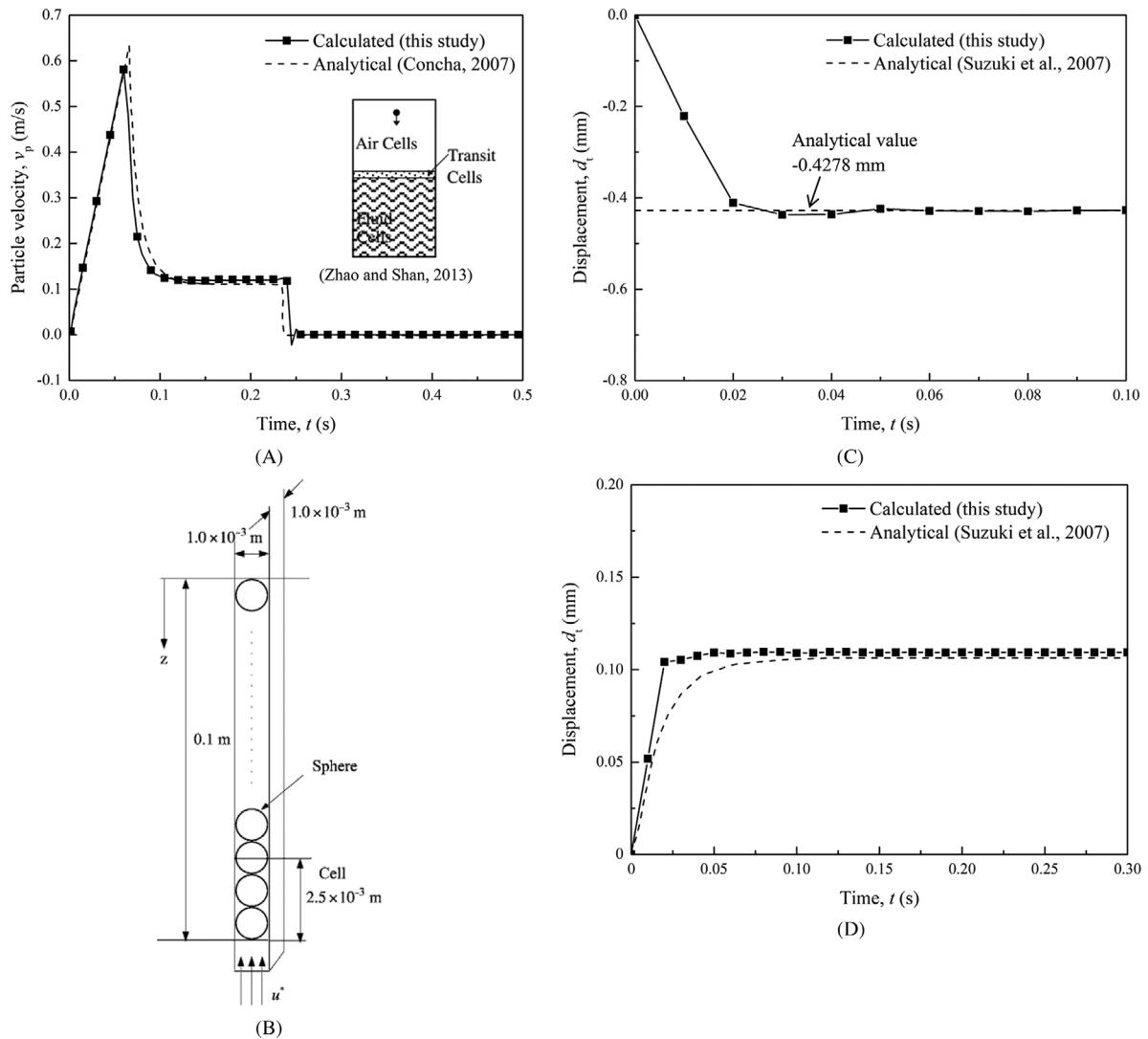
**FIGURE 2** (A) Comparison of the CFD-DEM prediction and the analytical solution for velocity of single-particle settling in water, (B) initial configuration of model, (C) displacements of top particle for input velocity of 0.005 m/s, and (D) calculated displacement under gravity and particle-fluid forces from initial tentative configuration

fluid-solid interaction for single- and multiparticle is validated against two classic benchmarking examples, ie, single spherical particle settling from air to water and upward seepage flow in a single column of spheres.

## 3.1 | Single spherical particle settling from air to water

Sedimentation, or settling of particle into water, involves different particle-fluid interaction forces (ie, drag force, pressure gradient force, and viscous force), which are suitable for validating the coupled CFD-DEM method. Concha[33] has given the analytical solution of the settling velocity of a sphere setting from air to water as follows:

$$u_p(t) = \frac{1}{18} \frac{(\rho_p - \rho_f)d_p^3 g}{\mu_f} \left[ 1 - \exp\left( -\frac{1}{27} \frac{\mu_f}{\rho_p d_p^3} t \right) \right], \qquad (9)$$

where $\rho_p$ and $\rho_f$ are the density of the particle and fluid, respectively.

In the benchmarking simulation, a spherical particle of $d_p = 1$ mm was dropped from a height of 45 mm from the center of a container (see inset of Figure 2A). The detailed information of the CFD-DEM model for this problem, including

model geometry and parameters, is obtained from Zhao and Shan.[34] Figure 2A compares the predicted and analytical results for the benchmarking example. It is evident that the predicted velocity of the particles in the water by the coupled CFD-DEM method is very similar to that calculated by the analytical solution, with a maximum percentage difference of smaller than 4.5%. This demonstrates the predictive capability of the CFD-DEM method for capturing the particle-fluid interaction force for a single particle.

## 3.2 | Upward seepage flow in a single column of spheres

The phenomena of suffusion can be presented by simulating the seepage flow on sphere packings. The problem of upward seepage flow in a single column of spheres is a highly idealistic model for evaluating the fluid forces acting on massive particles during suffusion. The analytical solution for the settlement of the highest spheres without seepage flow was developed by Suzuki et al,[35] as given below:

$$\delta = \frac{N(N+1)}{2k_n}\frac{4\pi}{3}\left(\frac{d}{2}\right)^3 (\rho_p - \rho_f)g, \tag{10}$$

where $N$ and $k_n$ are the number of particles and spring constant, respectively. $d$ is the diameter of each particle. After the injection of upward seepage flow with a velocity of 0.005 m/s, the analytical solution for the displacement of the highest spheres in the column is given below:[35]

$$
\begin{aligned}
S_t &= \frac{u^*}{C_v}\frac{H^2}{2}\left(1 - \frac{32}{\pi^3}\sum_{i=0}^{\infty}\frac{(-1)^i}{(2i+1)^3}e^{-T_v(2i+1)^2\pi^2/4}\right), \\
C_v &= \frac{k}{m_v\rho_f g}, \\
T_v &= \frac{C_v t}{H^2},
\end{aligned}
\tag{11}
$$

where $u^*$ is input flow velocity; $T_v$ is time factor; $C_v$ is the coefficient of consolidation; $k$ is the coefficient of permeability; $m_v$ is the coefficient of volume compressibility; and $H$ is the height of the column. The $m_v$ can be directly evaluated from the highly idealized model, while $k$ is deduced from the experimental results by Ergun[36] as follows:

$$k = \frac{u^*}{i} = \frac{\rho_f g}{\dfrac{1-n}{dn^3}\left\{150\dfrac{(1-n)\mu}{d} + 1.75\rho_f u^*\right\}}, \tag{12}$$

where $n$ is porosity. Figure 2B shows the initial tentative configuration of the CFD-DEM model for this problem. The model geometry and parameters involved in the CFD-DEM simulation are obtained from Suzuki et al.[35]

Figure 2C compares the predicted (by CFD-DEM method) and calculated (by Suzuki's analytical solution) settlement of the top particle without seepage flow. In this phase, the column of particles was only subjected to gravity and buoyancy. The calculated value was verified to be consistent with the theoretical value of $0.4278 \times 10^{-3}$ m derived from Equation (10). Figure 2D compares the simulated and analytical displacement of the highest particle after the injection of upward seepage flow at a velocity of 0.005 m/s. The simulated results are about 10% larger than the analytical solution. The reasonable agreement with the predicted and calculated results implicates that the coupled CFD-DEM method has an excellent performance in capturing interactions between fluid and multiparticles.

## 4 | SIMULATION PROGRAM AND MODEL SETUP

### 4.1 | Simulation program

The simulation in this study carried out 16 cases with typical range of $F_c$, $p'$, and $i$ to investigate their coupling effects on suffusion. Each gap-graded sample consists of particles with two diameters, ie, coarse particles ($D_c = 1.0$ mm) and
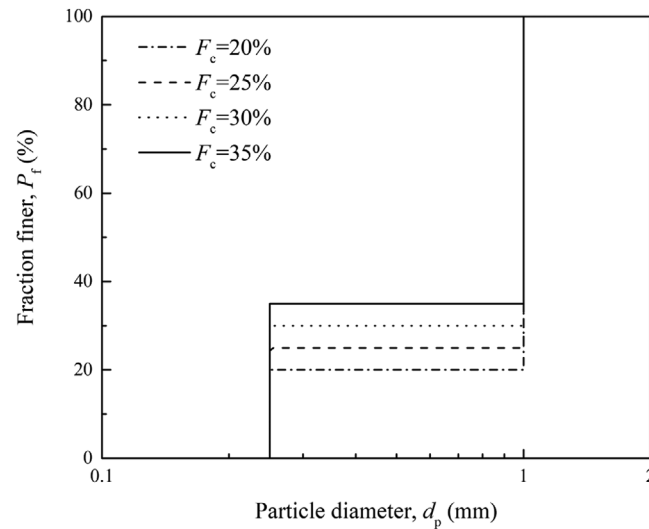
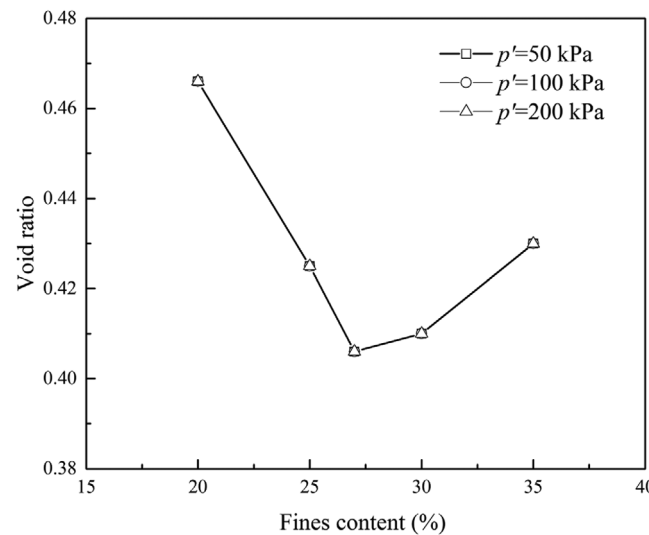**FIGURE 3** Particle size distributions of gap-graded samples analyzed in this study



**FIGURE 4** Variation of void ratio with fines content

fine particles ($d_f$ = 0.25 mm). The gap ratio $D_c/d_f$ = 4 was unstable according to the Kézdi method[37] and the Kenney and Lau criterion.[38] The low gap ratio and uniform diameter of the coarse and fine particles were adopted to reduce the total number of DEM particles for reasonable calculation efficiency. In the present study, the gap-graded soils are made up of monodispersed fine and coarse particles, which is indeed unusual in DEM simulations. Monodisperse materials are known to be prone to crystallization, particularly for samples with relatively low or high $F_c$. The reason of adopting such simple form of gap-graded soil (ie, monodispersed) without considering crystallization is to reduce the computation time of each CFD-DEM simulation, which took at least 5-7 days even for sample with monodispersed grading. The shear stress ($q$) and soil density are not considered in this study. Both of them also have significant effects on suffusion,[7,21–23] which could be analyzed in future work.

Four different combinations between the fine and coarse particles were considered, leading to four values of fine contents, ie, $F_c$ = 20%, 25%, 30%, and 35%. Figure 3 shows the particle size distribution of the four types of gap-graded samples used in the simulation. It is worth noting that for the material considered in this study, the fine content transition from underfilled to overfilled microstructure is around 27%, which was quantified through a series of parametric study considering different fine contents ($F_c$ = 20%, 25%, 27%, 30%, 35%) and confining stresses ($p'$ = 50, 100, and 200 kPa). The resulted void ratios of the gap-graded samples with the given combinations of $F_c$ and $p'$ are shown in Figure 4. It can be

**TABLE 1** Simulation program

| Simulation identity | Fines content, $F_c$ (%) | Confining pressure, $p'$ (kPa) | Hydraulic gradient, $i$ |
|---|---|---|---|
| FC20P50-IL | 20 | 50 | 0.2 |
| FC20P200-IL | 20 | 200 | 0.2 |
| FC35P50-IL | 35 | 50 | 0.2 |
| FC35P200-IL | 35 | 200 | 0.2 |
| FC20P50 | 20 | 50 | 2 |
| FC20P100 | 20 | 100 | 2 |
| FC20P200 | 20 | 200 | 2 |
| FC25P50 | 25 | 50 | 2 |
| FC25P100 | 25 | 100 | 2 |
| FC25-P200 | 25 | 200 | 2 |
| FC30P50 | 30 | 50 | 2 |
| FC30P100 | 30 | 100 | 2 |
| FC30P200 | 30 | 200 | 2 |
| FC35P50 | 35 | 50 | 2 |
| FC35P100 | 35 | 100 | 2 |
| FC35P200 | 35 | 200 | 2 |

seen that the fine content threshold (corresponding to the minimum void ratio, or the maximum packing efficiency) for the material considered is 27%, irrespective of the $p'$ value. Similar quantitative conclusion (ie, fine content threshold is approximately 25%) was also made by the previous DEM studies.[9] It was further revealed by these studies that for samples with $F_c < 25\%$, the fine particles underfill the voids between coarse particles and play a diminished role in stress transfer. In contrast, when $F_c > 25\%$, the fine particles start to overfill the voids between coarse particles, exerting a significant effect on the entire force network of the sample.

A relatively lower and higher hydraulic gradients, $i = 0.2$ and 2 ($i = \triangle p/\rho gL$, where $\triangle p$ is the differential pressure and $L$ is the sample length along the flow direction) were considered in this study to incorporate the effect of $i$ on the evolution of suffusion. Three different levels of confining pressure were imposed on each sample under $i = 2$. When $i = 0.2$, high and low levels of confining pressure were imposed on the samples with $F_c = 20\%$ and 35%. Table 1 summarizes the details of the simulation program.

## 4.2 | Model geometry and parameters

Figure 5 shows a cubical permeameter test with stress-controlled boundaries simulated using the coupled CFD-DEM method. The length of the cubical sand sample was about 13.5 mm under $p' = 50, 100, 200$ kPa. The CFD domain overlaps the DEM domain with the size of 14.5 mm × 14.5 mm × 19.0 mm, ensuring it entirely covering the DEM domain. The size of each fluid mesh is 2.9 mm × 2.9 mm × 3.2 mm, which is approximately 1.5-6.4 times of the particle diameter (ie, 2.0 mm and 0.5 mm for the coarse and fine particles, respectively). As the fluid mesh is much larger than the grain size, the coupled CFD-DEM approach used in this study is spatially unresolved. The contact model between particles is the Hertz contact law, of which the adopted parameters in this study are approved to be appropriate for simulating sand.[39] The fluid parameters are widely used water parameters in previous study.[34] Table 2 summarizes the properties of particles and fluid and numerical settings in the simulations.

To achieve numerical stability for CFD and DEM domain, the Courant number, defined in Equation (13), should be below 0.2 and the time step for DEM domain should be determined by the method proposed by Cundall and Strack[40] as seen in Equation (14).

$$C = \frac{\mathbf{U}^f \Delta t_f}{\Delta l}, \tag{13}$$

**FIGURE 5** Coupled DEM-CFD simulation for internal erosion (particles are colored by radius and the CFD grid is overlain in blue)
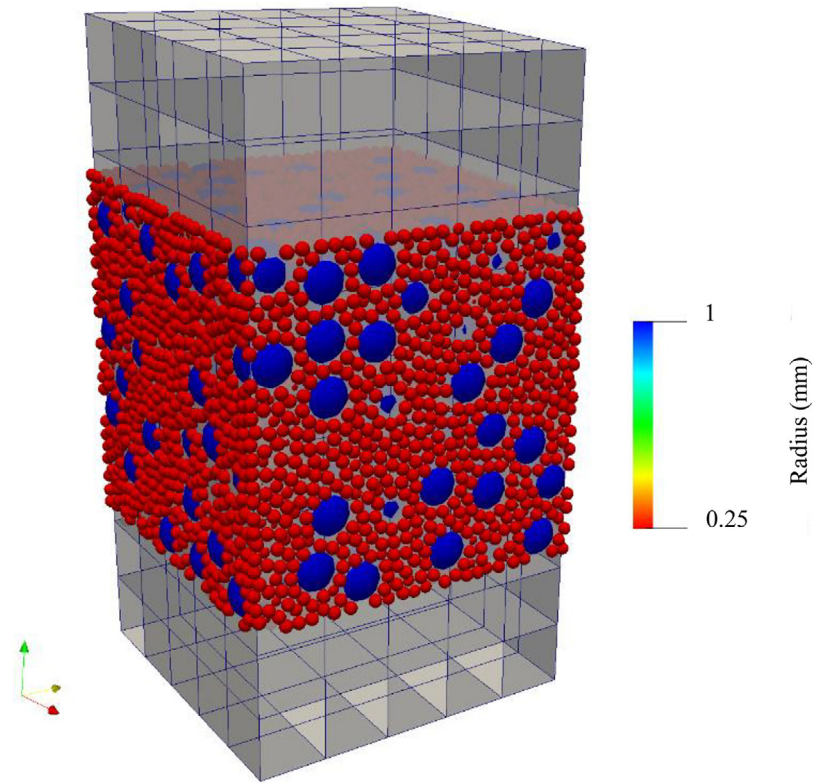


**TABLE 2** Summary of model parameters

| | Model parameters | |
|---|---|---|
| Physical model | Sample dimensions $L \times W \times H$ (mm) | $15 \times 15 \times 15$ |
| | Simulation time (seconds) | 14.0 |
| CFD | Cells | $5 \times 5 \times 9$ |
| | Fluid viscosity, $\mu$ (Pa·s) | $1 \times 10^{-3}$ |
| | Density, $\rho_f$ (kg/m$^3$) | 1000 |
| DEM | Elastic modulus, $E$ (GPa) | 7 |
| | Poisson's ratio, $\nu$ | 0.3 |
| | Coefficient of restitution, $e$ | 0.7 |
| | Friction coefficient, $\mu_f$ | 0.3 |
| | Rolling friction coefficient, $\mu_r$ | 0.1 |

where $\Delta t_f$ is the fluid timestep and $\Delta l$ is the minimum fluid cell length.

$$\Delta t \leq 2\sqrt{\frac{M}{k}}, \tag{14}$$

where $M$ and $k$ are the lowest particle mass of the compact and contact stiffness, respectively. $\Delta t$ is the timestep for DEM domain. In this study, the fluid timestep was adopted as $1.0 \times 10^{-4}$ seconds, ensuring that Courant number of all the simulations was an order of $10^{-3}$ that was low enough to ensure numerical stability for CFD. For the typical mass, size, and stiffness considered in this study, the time step calculated from Equation (14) is approximately $5 \times 10^{-7}$ seconds. For the parameters in Table 2, it can be readily calculated that the maximum particle Reynolds number (Re$_p$) under a typical hydraulic gradient of $i = 2$ is 5.6. This means the flows simulated in all the analyses reported herein fell within the laminar range (Re$_p < 10$).

## 4.3 | Boundary conditions

In the permeameter experiment, the hydraulic gradient along the soil sample was controlled by the fluid pressure at the inlet and outlet of the apparatus. The fluid pressures within the upstream and the downstream CFD domains with no grains are constant. The pressure gradient ($i$) seen by each sample is given by the imposed pressure drop divided by the granular sample length, which was remained either 0.2 or 2 during suffusion. Since gravity forces were not considered, $i$ was simply a dimensionless rescaling of $\triangle p$.[22] The free slip boundary condition was applied on each lateral boundary, meaning that the surface fluid was restricted to move along the lateral boundaries.

For the boundary conditions of the DEM, isotropic stress ($p' = 50$, 100, and 200 kPa) was applied to each boundary of each particle specimen using a servo wall algorithm. The confining wall was assumed to be rigid and perfectly smooth (ie, $\mu_{wall} = 0$), with its normal stiffness being 10 times larger than that of particles. The bottom of each specimen was supported vertically by a downstream wall, which was fixed in both vertical and horizontal directions. To allow the escape of the eroded particles from the samples, a series of holes with size 0.875 mm × 0.875 mm (1.75 times the fine particle diameter) was set at an equal spacing (0.125 mm) on the downstream wall.

## 4.4 | Simulation procedure

Each cubic assembly of spheres was first generated randomly with the prescribed gradation as shown in Figure 3 and isotopically loaded by six surrounding walls to the target level of confining pressure. The interparticle friction coefficient was maintained at a relatively low value of 0.1 during the sample preparation processes (ie, generating particles and applying confining stress to the sample), with the intention to produce medium dense samples. The resulted relative densities of the samples are in the range between 58.8% and 70.2%. The relative density of each sample is calculated by the following equation:

$$R_d = (e_{max} - e) / (e_{max} - e_{min}), \tag{15}$$

where $e$ is the void ratio of the sample and $e_{max}$ and $e_{min}$ are the maximum and minimum void ratios of the sample, respectively. Following Salot et al[41]'s method, the minimum and maximum void ratios are achieved by setting the coefficients of interparticle friction $\mu = 0.0$ and 1.0 during the isotropic compression stage of the least and the most dense samples, respectively.

After the sample preparation and before applying seepage flow, the interparticle friction coefficient is increased to 0.3. The unbalanced force within the DEM samples, which was defined in Equation (16), was found to stay below 0.01[22] before the initiation of the suffusion simulation.

$$F_{unb} = \frac{\frac{1}{N_p} \sum_{p=1}^{N_p} \left\| F_p \right\|}{\frac{1}{N_c} \sum_{c=1}^{N_c} \left\| F_c \right\|}, \tag{16}$$

where $F_p$ is the sum of all contact forces acting on particle $p$ and $F_c$ is the contact force between two particles. $N_p$ and $N_c$ are the number of particles and contacts, respectively. After generation of the initial DEM sample, a differential hydraulic pressure was imposed on the upstream and downstream of each gap-graded sample to model suffusion. Table 3 summarizes the number of simulated particles and micromechanical properties of each sample, including fines content, void ratio, and relative density.

During each simulation, the pressure applied to the six surrounding walls of each sample remained constant. The particles that flowed out of the downstream wall were deemed as eroded particles. The information for all particles (including position, velocity, drag force, etc.) and all contact forces and energies within the samples were all recorded into files at every 0.05 seconds during each suffusion simulation with a total duration of 14.0 seconds. Each simulation that model 14 seconds of physical time of suffusion in this study took approximately 5-7 days on a HP station with 8 Intel Xeon E52680-v4 2.4 GHz processors and 512 GB DDR4 RAM. Although the simulation duration is relatively short (ie, 14 seconds) as compared with that in a laboratory test, this duration has largely covered the key stages for suffusion involved in each analysis,

**TABLE 3** Number of simulated particles and micromechanical properties of each sample

| Simulation identity | Fines content (%) | No. of total particles | No. of coarse particles | No. of fine particles | Void ratio, $e$ | Relative density, $R_d$ (%) |
|---|---|---|---|---|---|---|
| FC20P50 | 20 | 9926 | 587 | 9339 | 0.46 | 58.8 |
| FC20P100 | 20 | 9944 | 587 | 9357 | 0.46 | 58.8 |
| FC20P200 | 20 | 9968 | 587 | 9381 | 0.46 | 58.8 |
| FC25P50 | 25 | 9902 | 447 | 9455 | 0.44 | 62.4 |
| FC25P100 | 25 | 9931 | 447 | 9484 | 0.44 | 62.4 |
| FC25P200 | 25 | 9953 | 447 | 9506 | 0.44 | 62.4 |
| FC30P50 | 30 | 9846 | 351 | 9495 | 0.42 | 66.1 |
| FC30P100 | 30 | 9906 | 351 | 9555 | 0.42 | 66.1 |
| FC30P200 | 30 | 9972 | 351 | 9621 | 0.42 | 66.1 |
| FC35P50 | 35 | 9845 | 280 | 9565 | 0.41 | 70.2 |
| FC35P100 | 35 | 9904 | 280 | 9624 | 0.41 | 70.2 |
| FC35P200 | 35 | 9951 | 280 | 9671 | 0.41 | 70.2 |

ie, initiation, intensified suffusion following initiation, and a gradually stabilized response. In other words, each simulation reported herein has contained key macro- and microscopic mechanisms on the suffusion of gap-graded soil. On the other hand, the short physical time is sufficient to describe suffusion in DEM because the numerical sample dimension is very small (ie, the length is about 13.5 mm) compared with that of the experimental sample (ie, the length is about 100-150 mm). A sample of the "numerical dimensions" inside a real lab sample would see some perturbations coming from the rest of the sample during the suffusion test (eg, input of new particles in the upstream, modification of the stress state, etc.). As a result, the final state is longer to reach in the experiments.

# 5 | SIMULATION RESULTS

## 5.1 | Macroresponses of the gap-graded samples to suffusion

Figure 6A shows the percentage of cumulative fines loss with time for the samples having different initial fines contents ($F_c$ = 20% and 35%) and confining pressures subjected to a given hydraulic gradient of 0.2. Only results for the sample with $F_c$ = 20% and 35% were illustrated because the critical fines content at which the fines fill the voids is about 27% for the sample considered in this study. It is noted that the cumulative fines loss was decreased with confining pressure for all samples, meaning that high confining pressure helped to resist the erosion of fines caused by seepage flow with a relatively low hydraulic gradient. Many previous studies[4–7,12] have also confirmed this observation, attributing it to stronger contact forces between particles imposed by high confinements.[9] The load-bearing skeleton of the sample was relatively stable under the condition of a low hydraulic gradient, so that only fines with small contact forces were eroded. Figures 6B and C show that no excessive deformation for each sample was observed under the condition of $i$ = 0.2, meaning that the load-bearing skeleton of each sample was stable during suffusion.

However, if $i$ was increased to a sufficiently large value to destabilize the original load-bearing skeleton (usually occurs in backward erosion), the confining pressure was found to intensify suffusion. Figure 7A shows the percentage of cumulative eroded particles for the samples with $F_c$ = 20% (ie, fines underfilled the voids between coarse grains) and 35% (ie, fines overfilled the voids between coarse grains) under $p'$ = 50, 100, and 200 kPa when $i$ = 2.0. In contrast with the results when $i$ = 0.2, the cumulative eroded soil mass for all samples increased with the effective confining pressure, meaning that the confining pressure facilitated the transportation and erosion of the fine particles, especially for the sample with $F_c$ = 35% (ie, fines overfilled the voids between coarse grains). This is probably because the fines overfilled the voids between coarse particles and participated heavily in load-bearing for the sample with $F_c$ = 35%. The erosion of fines under high $i$ could cause the collapse of the original force transmission structure. The release of higher strain energy within samples under higher $p'$ accelerated particle movement and intensified suffusion. Detailed micromechanical analyses are
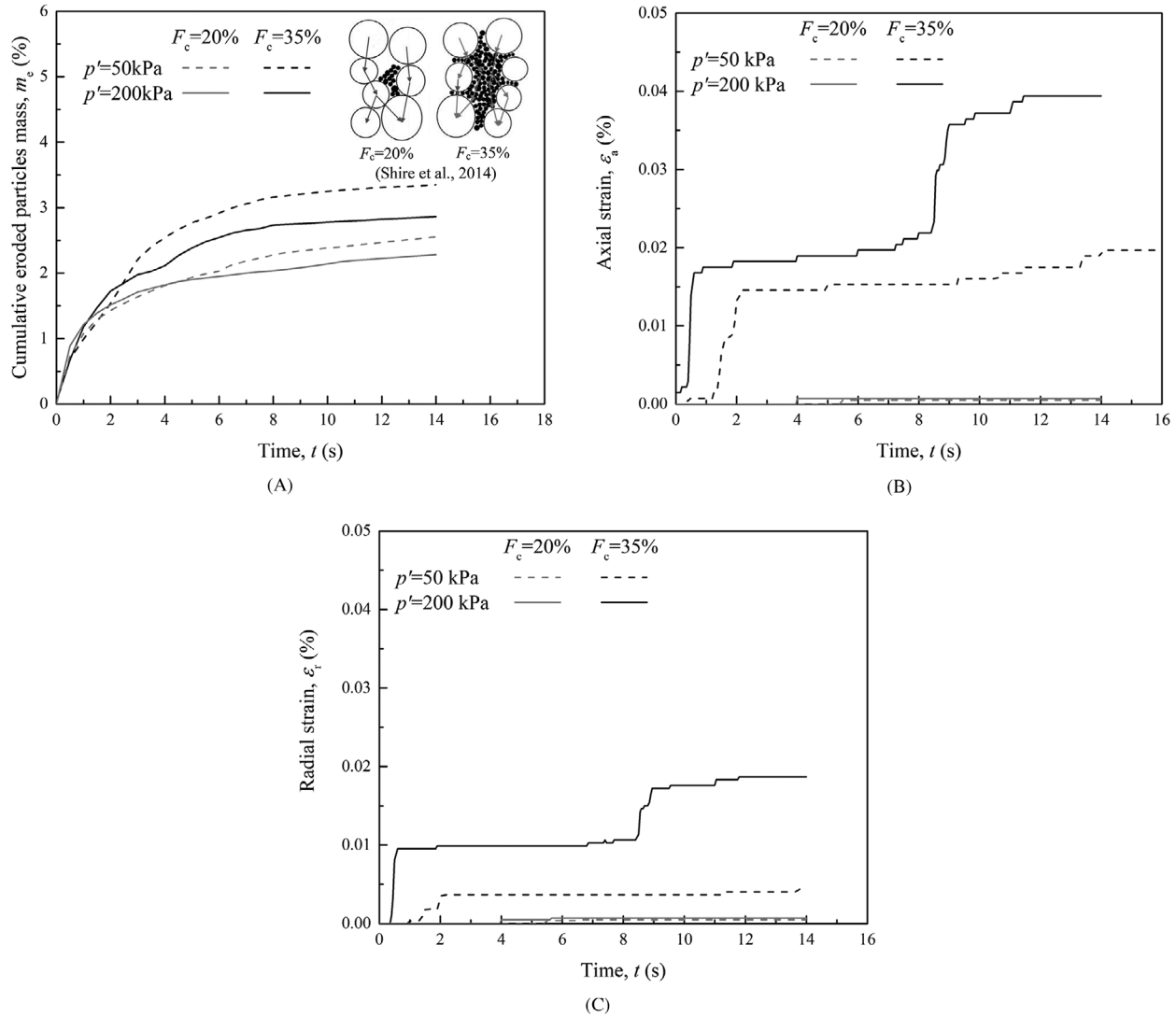
**FIGURE 6** Simulation results for the samples with $F_c$ = 20% and 35% under $i$ = 0.2 and $p'$ = 50 and 200 kPa: (A) cumulative eroded soil weight percentage, (B) axial strain, and (C) radial strain

given in Sections 5.2-5.4. This tendency is in accordance with the experimental findings made by Tomlinson and Vaid,[1] Papamichos,[2] Bendahmane et al,[3] and Chang.[42]

The curves for the sample with $F_c$ = 35% (ie, fines overfilled the voids between coarse grains) under $i$ = 2.0 indicate that after the initiation of suffusion, the eroded particles mass and deformation of the sample both increase dramatically. Figure 8A-D show the axial and radial deformation of each sample under $i$ = 2.0, which are consistent with the corresponding cumulative eroded particles mass. The moment for the sudden increase of eroded fines loss and the sample deformation in the case of $F_c$ = 30% and 35% (see Figures 7 and 8) is called turning point in this study. The basic physical cause of the turning point is the strong force chain buckling and the associated collapse of the force transmission structure of the sample, with a substantial increase in the eroded fines loss and the appearance of significant kinetic energy of total particles. A detailed analysis of the physical cause of the turning point is given in Sections 5.3 and 5.4. The subsequent analyses will focus on the effects of confining pressure on the suffusion behavior of the samples containing different fines contents under $i$ = 2.0.

To check if a regressive erosion occurs in the simulations of this study, Figure 9 shows the vertical profile of fines content before and after erosion for the samples with $F_c$ = 20% and 35% under $p'$ = 50 kPa. It can be observed that the fine particles in the top four layers are migrated from the upstream to the downstream region during suffusion, suggesting that the regressive erosion is not likely to occur within the whole sample. The particles at the bottom layer are significantly eroded due to the circular holes in the downstream confining wall.
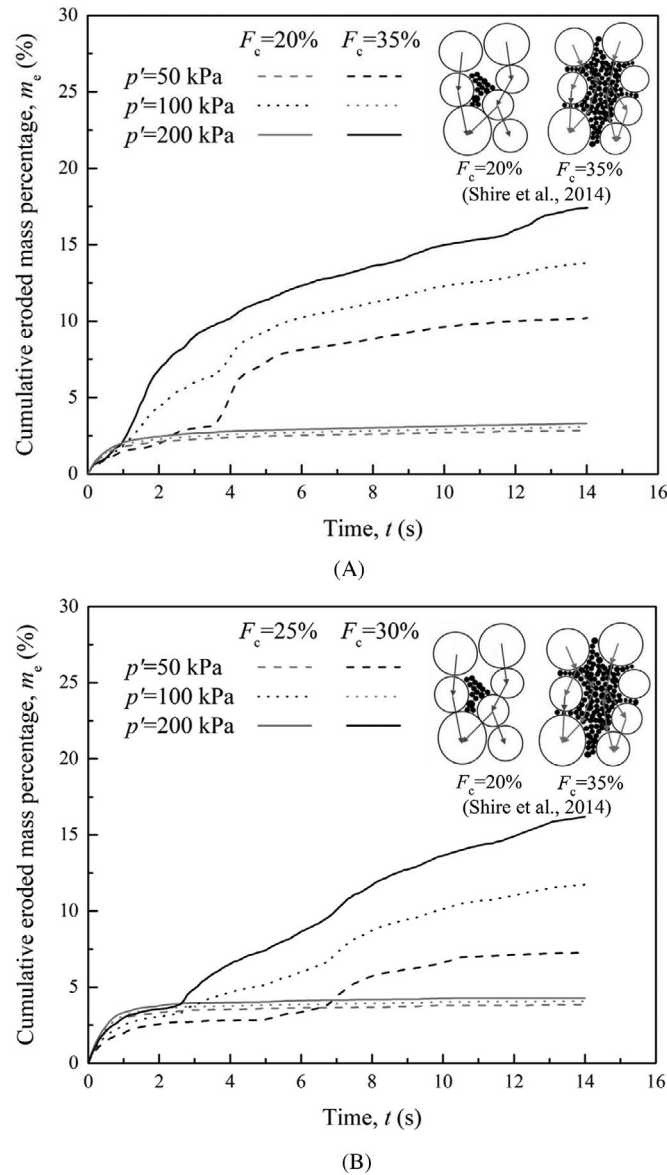
**FIGURE 7** Cumulative eroded mass percentage for the sample with: (A) $F_c = 20\%$ and $35\%$ and (B) $F_c = 25\%$ and $30\%$ under $i = 2.0$ and $p' = 50$ and $200$ kPa

Two distinct macroresponses to confining pressure for the sample with $F_c = 20\%$ (ie, fines underfilled the voids between coarse grains) and $35\%$ (ie, fines overfilled the voids between coarse grains) stem from the structure of the soil packings as shown in the inset of Figure 7. For the samples with $F_c = 35\%$ (ie, fines overfilled the voids between coarse grains), the fines overfill the voids between coarse particles, separating the coarse particles and forming a load-bearing skeleton. In this case, the erosion of fines has significant effects on the entire force network of the sample. While for the samples with $F_c = 20\%$ (ie, fines underfilled the voids between coarse grains), the fines underfill the voids between coarse particles with little contribution to the load-bearing skeleton. Even though the fine particles were gradually eroded under $i = 2.0$, the original load-bearing skeleton remains stable, which was similar to the condition of $i = 0.2$. Figure 7B shows that the suffusion behavior for the samples with $F_c = 25\%$ (ie, fines underfilled the voids between coarse grains) and $30\%$ (ie, fines overfilled the voids between coarse grains) has a similar tendency stated above.

In order to further understand the characteristics of the two typical structures of soil packing, Figures 10 and 11 show the initial sample profile, contact force, and strain energy for the samples with $F_c = 20\%$ (ie, fines underfilled the voids between coarse grains) and $F_c = 35\%$ (ie, fines overfilled the voids between coarse grains) under $p' = 50$ and $200$ kPa. The strain energy of each contact consists of a normal ($E_{sn}$) and a shear component ($E_{st}$), which are calculated by Equations (16)
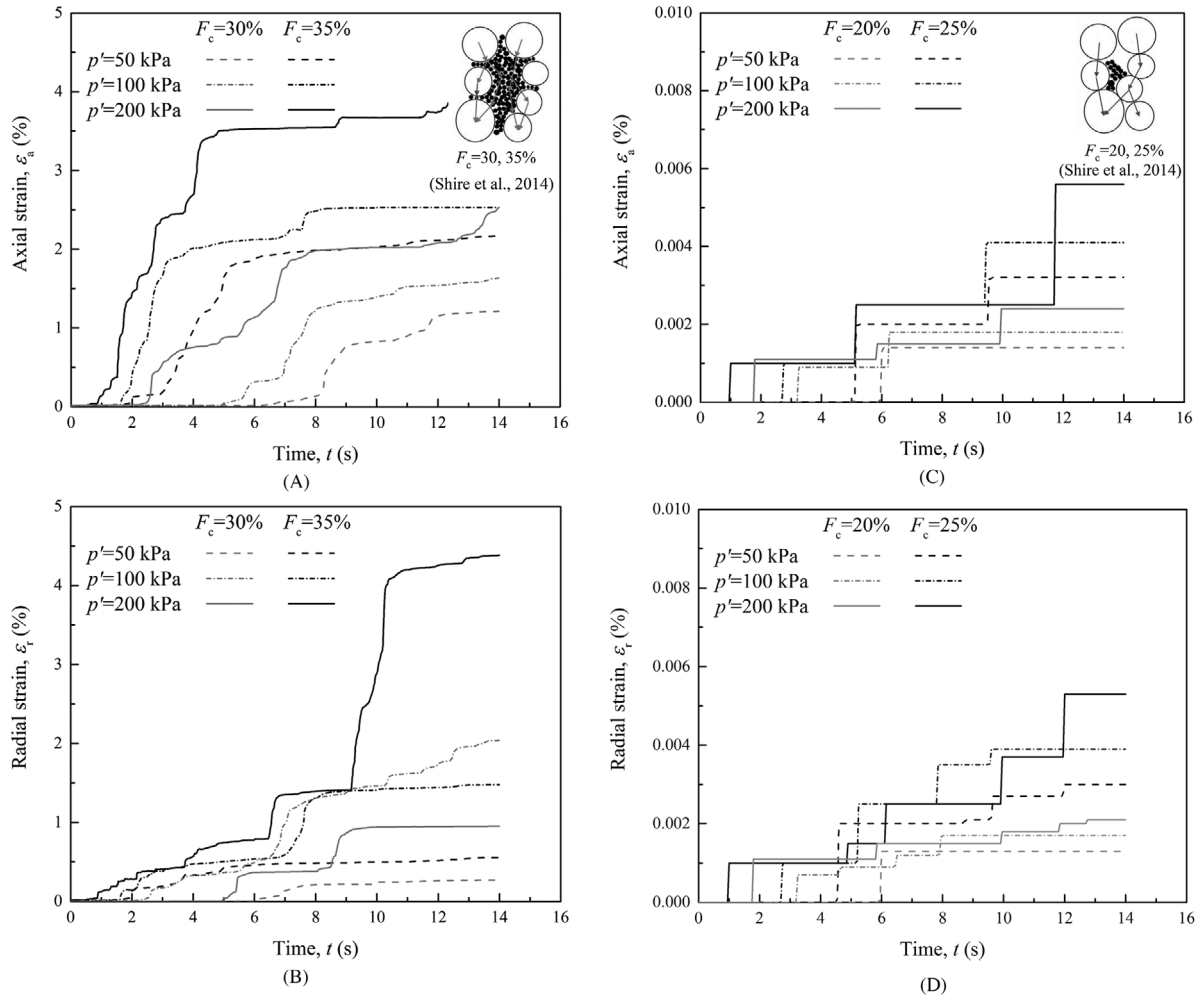
**FIGURE 8** (A) Axial strain and (B) radial strain for the samples with $F_c = 30\%$ and 35%; (C) axial strain and (B) radial strain for the samples with $F_c = 20\%$ and 25% under $i = 2$ and $p' = 50$, 100 and 200 kPa
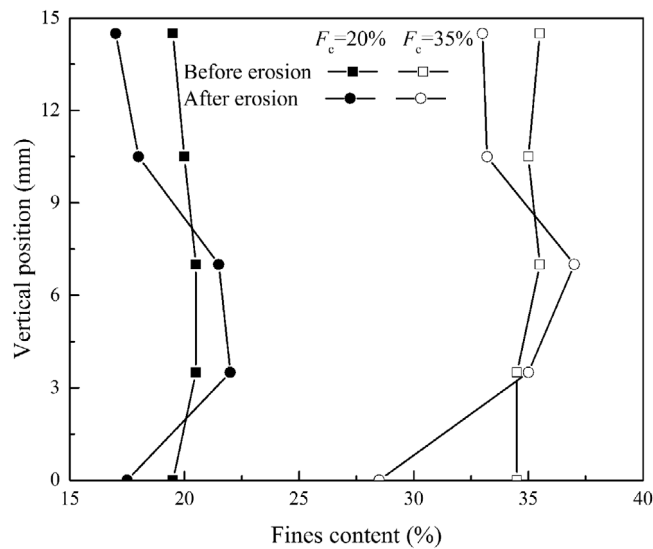


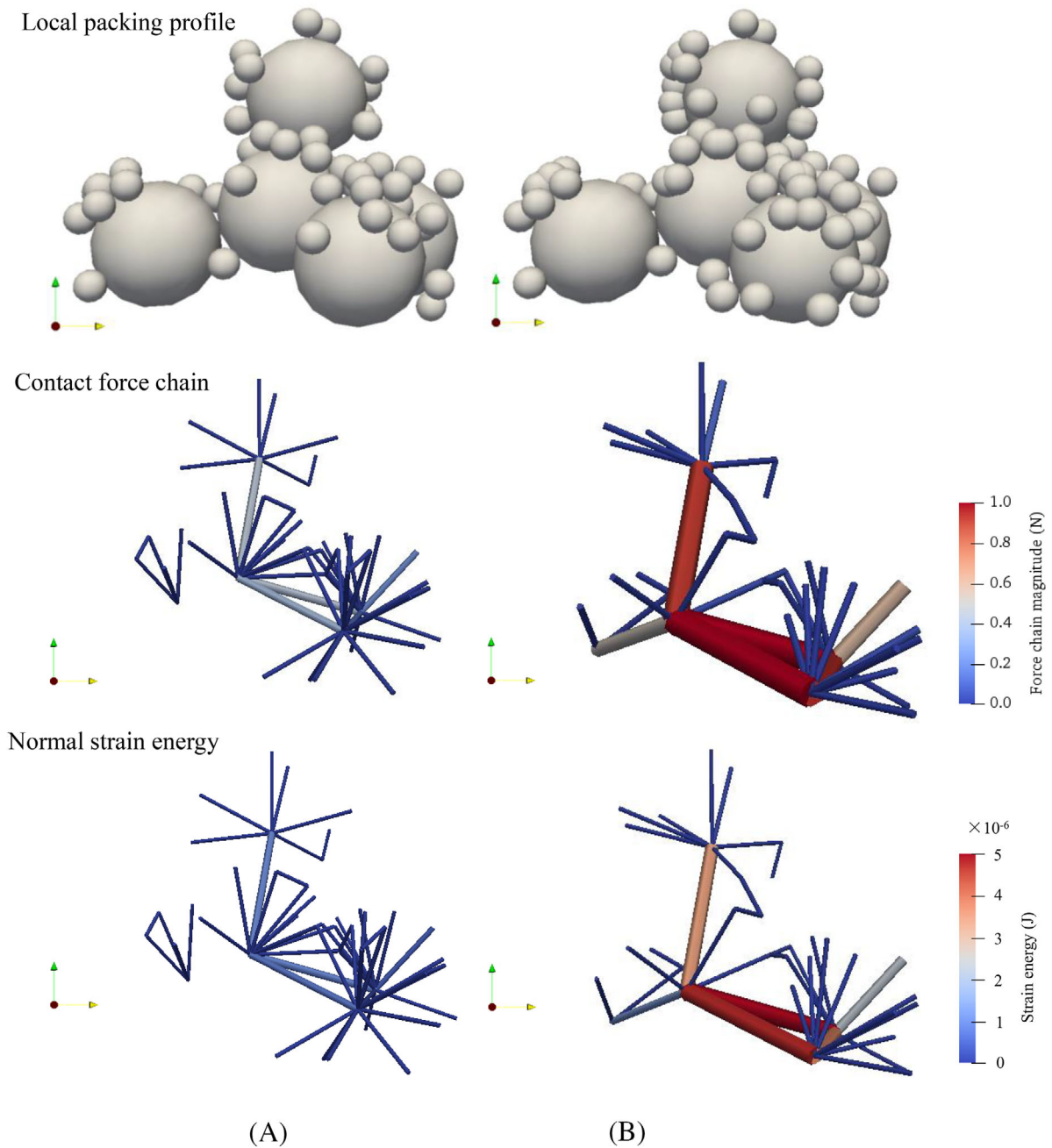**FIGURE 9** Vertical profile of fines content for the samples with $F_c = 20\%$ and 35% before and after erosion

Local packing profile



Contact force chain



Normal strain energy



(A)                                         (B)

**FIGURE 10** Initial profile, contact force chain, and normal strain energy of local packing for the sample with (A) $F_c = 35\%$ and $p' = 50$ kPa and (B) $F_c = 35\%$ and $p' = 200$ kPa

and (17), respectively[43]:

$$E_{sn} = \frac{2}{5} |F_n| s, \tag{17}$$

$$E_{st} = E_{st}^{\beta-1} + \frac{\left|F_t^{\beta-1} + F_t^{\beta}\right|}{2} \frac{\left|F_t^{\beta} - F_t^{\beta-1}\right|}{k_t}, \tag{18}$$

where $F_n$ and $s$ are the normal force and interparticle overlap of the contact, respectively. $E_{st}^{\beta-1}$ is the tangential component of strain energy at previous time step $\beta$-1. $F_t^{\beta}$ and $F_t^{\beta-1}$ are the tangential force of the contact at current and previous time steps, respectively. $k_t$ is the contact shear tangential stiffness. It is observed from Figures 11 and 12 that for the samples
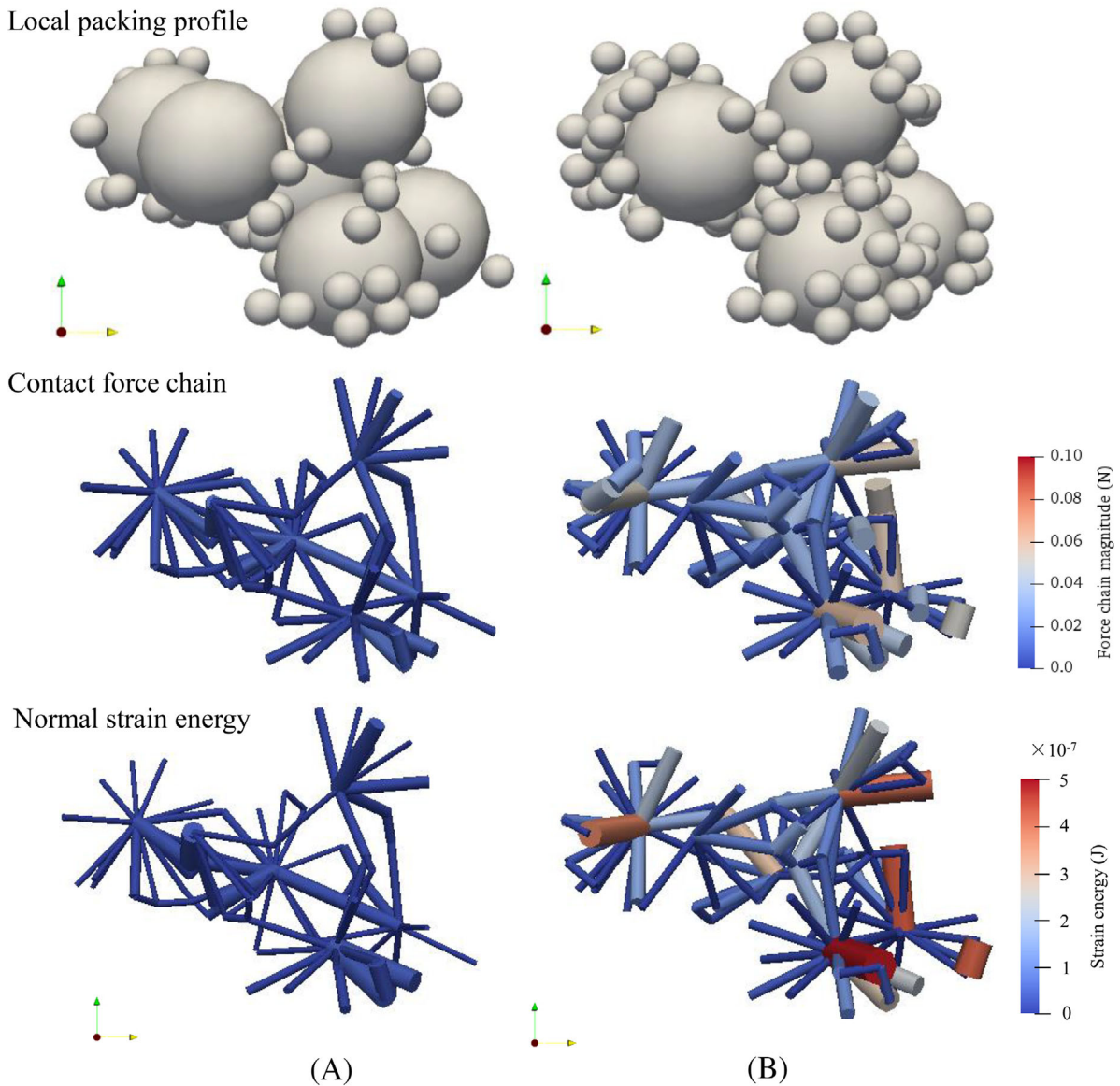
Local packing profile



Contact force chain

Normal strain energy

(A)                    (B)

**FIGURE 11** Initial profile, contact force chain, and normal strain energy of local packing for the sample with (A) $F_c = 20\%$ and $p' = 50$ kPa and (B) $F_c = 20\%$ and $p' = 200$ kPa

with $F_c = 35\%$ (Figure 12), the contacts with larger forces contain more strain energy. The fines overfill the voids between coarse particles, separating the coarse particles and forming a load-bearing skeleton. In this case, the erosion of fines has significant effects on the entire force network of the sample. If the load-bearing skeleton of the samples collapses, more fines will be eroded[3,12] owing to the weakened contact forces acting on fines and the release of strain energy stored in these contacts. The collapse of stronger contact forces within samples under higher $p'$ causes more strain energy to release that will intensify suffusion (detailed analysis in Section 5.4).

While for the samples with $F_c = 20\%$ (ie, fines underfilled the voids between coarse grains), the profile of contact forces (Figure 11) shows that the magnitude of coarse-fine contact forces is small, which implies that fines underfill the voids between coarse particles with little contribution to the load-bearing skeleton.[42,44] The external force of the soil skeleton is mainly transmitted by coarse particles,[45] which means that $p'$ hardly influences the number and magnitude of contact forces acting on fines. Thus, the loss of fines due to suffusion is slightly affected by $p'$. Novel ground improvement techniques such as microbially induced calcite precipitation (MICP) may help to prevent suffusion of gap-graded soils.[46,47]
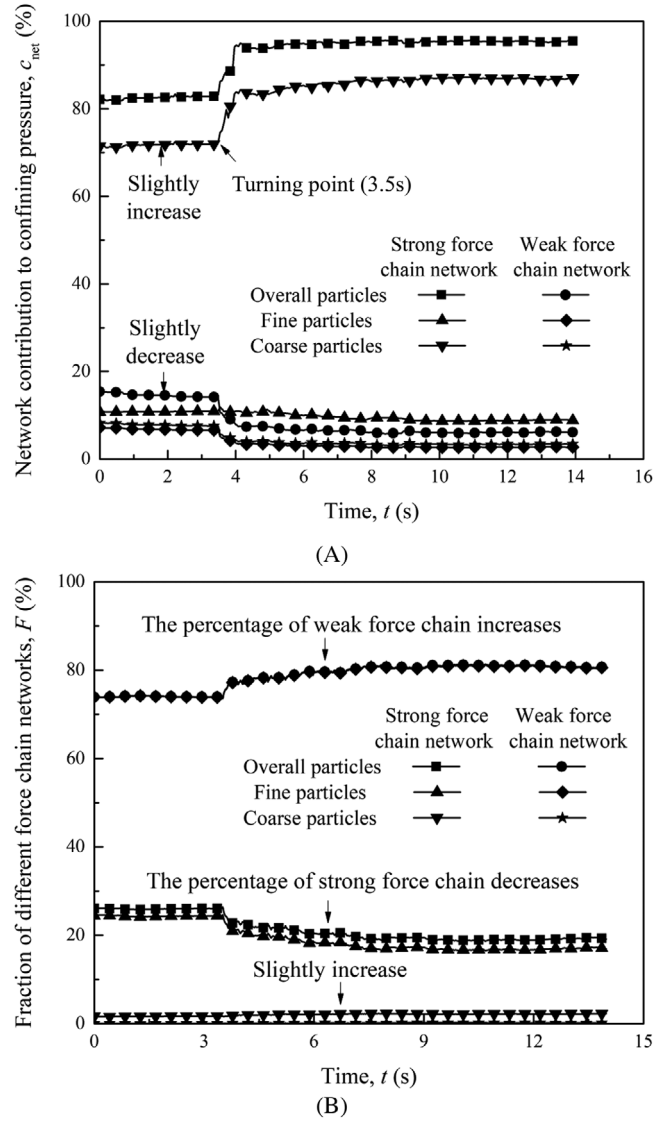
**FIGURE 12** Characteristics of the force chain networks for the samples with different $F_c = 35\%$ and $p' = 50$ kPa: (A) network contribution of confining pressure and (B) fraction of different force chain networks (the fraction of the weak force chain networks formed by overall particles and fine particles is coincided)

## 5.2 | The role change of different networks during suffusion

The contribution of various contact networks to the overall external confining pressure, which is calculated by Equation (19), can be used to reflect the mechanical consequences of suffusion for different fractions within a sample.

$$c_{net} = p'_{net}/p',$$

$$p'_{net} = \frac{1}{3}\sigma_{ii},$$

$$\sigma_{ij} = \frac{1}{V} \sum_{c \in net} f_i^c d_j^c,$$

(19)

where *net* denotes the different strong or weak networks formed by the overall contacts, coarse-coarse/fine contacts, or fine-fine contacts. Coarse-coarse/fine contacts denote the meeting of the coarse-coarse and coarse-fine contacts. $p'_{net}$ is the confining pressure constituted by a network. $c_{net}$ means the contribution of a network to the overall confining pressure. $V$ is the total volume of the assembly. In this study, the average normal forces $(\overline{f}_n)$ are used to distinguish the strong and

weak networks.[48,49] $f_i^c$ is the contact force at a contact and $d_j^c$ is the branch vector joining the centers of two contacting particles.

Figures 12A and B show that the contribution and the fraction of various contact networks to confining pressure in the process of suffusion, respectively, for the samples with $F_c = 35\%$ (ie, fines overfilled the voids between coarse grains) under $p' = 50$ kPa and $i = 2.0$. For this kind of sample, the contribution of the weak network constituted by the fine-fine contacts decreased before turning point, while the contribution of the strong network constituted by the coarse-coarse/fine contacts increased, leading to a change in contribution of the overall strong and weak network to confining pressure. This is because in this phase, the fines with low connectivity and contact forces were eroded first,[15,16] resulting in stronger contact forces within the overall strong network.

After the turning point, Figures 12A and B show that both the contribution and the fraction of the overall strong network experienced a sudden change. The contribution of the strong network increased significantly (Figure 12A), whereas the fraction of the strong network decreased (Figure 12B). The weak network of the whole sample displayed the opposite trend. Another important fact is that after the turning point coarse, particles played a more important role in the load-bearing skeleton, as shown in Figure 12A, and the fine-fine contact forces were weakened. This is validated by Figure 12B, which shows that the fraction of strong network constituted by fine-fine contacts decreased. These trends are consistent with the study by Minh et al,[45] revealing that the contribution of fine-fine strong contacts reduced rapidly with the decrease of fines content while the contribution of the coarse-coarse/fine contacts increased.

For the sample with $F_c = 20\%$ (ie, fines underfilled the voids between coarse grains) under $p' = 50$ kPa and $i = 2.0$, Figure 13A illustrates how the contribution of different networks to the confining pressure remained constant during suffusion, meaning that the erosion of fines had little influences on the load-bearing skeleton. Figure 13B shows that the fraction of different networks for the sample also changed slightly during suffusion.

## 5.3 | Strong force chain buckling

In comparison with the sample with $F_c = 20\%$ (ie, fines underfilled the voids between coarse grains), the contribution and the fraction of the strong and weak networks for the sample with $F_c = 35\%$ (ie, fines overfilled the voids between coarse grains) experienced a sudden change during suffusion (Figure 7), after which the original load-bearing skeleton collapsed and a new skeleton was eventually formed. The collapse of the original load-bearing skeleton was mainly induced by the strong force chain buckling. Figures 14 and 15 show the evolution of the local specimen profile and the contact force chains during suffusion at the same position of the samples with $F_c = 20\%$ and $F_c = 35\%$, respectively. The strong force chains and the chained particles are marked in red. The strong force chain was defined in this study as three particles connecting in a quasi-linear mode, as shown in Figure 14, where the contact forces between particles were larger than the average value. According to Tordesillas[50] and Tordesillas et al,[51] force chain buckling occurs if the intersection angle of the chains is reduced by 1° in a short time (ie, $\delta t = 0.001$s). In this study, the above geometry variation criterion together with 50% reduction of the force chain magnitude was adopted to define strong force chain buckling. The particles in contact with the chained particles were also plotted to show the consequences of strong force chain buckling to the neighboring particles. Figure 14 shows that for the sample with $F_c = 35\%$ (ie, fines overfilled the voids between coarse grains), the magnitude of strong force chain increased obviously from the initial time to the turning point, implying that the external force was transferred from the weak contact forces to the strong contact forces due to the fines loss. This is consistent with the observed increase in the confining pressure of the strong network, as shown in Figure 12A. At the turning point, for the sample with $F_c = 35\%$ (ie, fines overfilled the voids between coarse grains), the coarse particle deviated from its original position in a short time, accompanying an apparent decrease in the angle between the strong force chains. At the same time, the magnitude of the force chain became minor. Such angel deflection and decrease of force chain magnitude are main characters of force chain buckling.[50,52]

Figure 15 shows the evolution of local specimen profile during suffusion for samples with $F_c = 20\%$ (ie, fines underfilled the voids between coarse grains). It should be noted that the local specimen profile as shown in Figures 14 and 15 were located in the same area of the respective samples. In this case, the bearing load skeleton was primarily constituted by coarse-coarse contacts (Figures 10A and B). The fines only underfilled the voids between coarse particles and their erosion had little influences on the strong coarse-coarse contacts. Figure 15 shows that the strong force chain marked in red was stable throughout the suffusion process. This was in accordance with the previous analysis that the role of the strong network slightly changed during suffusion in this case.
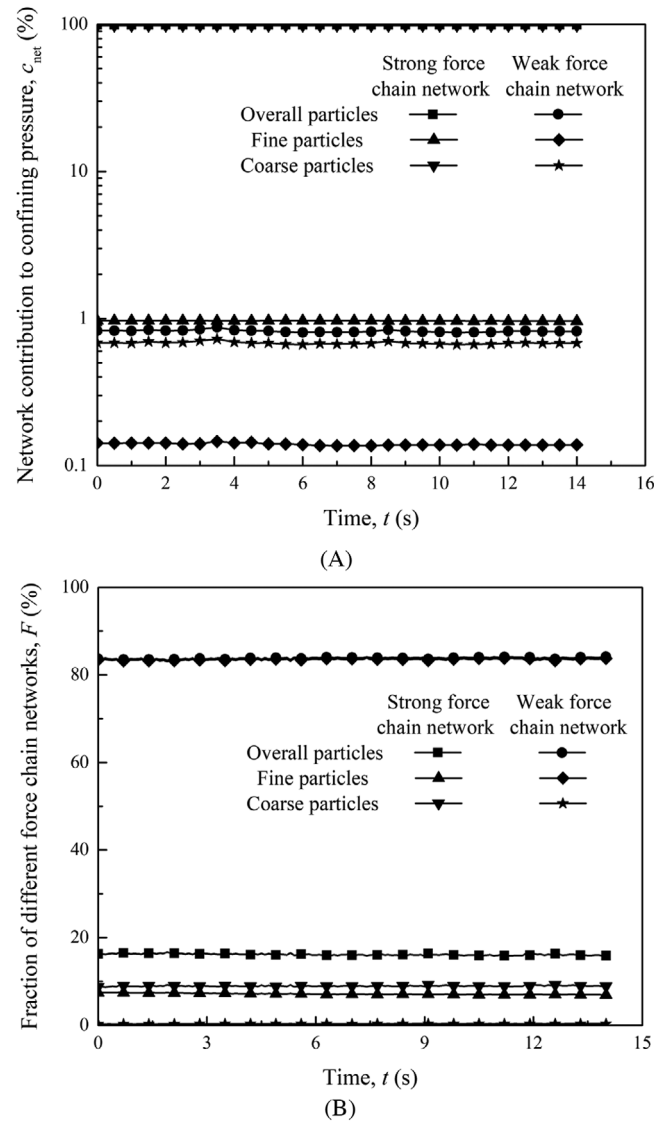
**FIGURE 13** Characteristics of erosion for the samples with different $F_c = 20\%$ and $p' = 50$ kPa: (A) network contribution of confining pressure and (B) fraction of different force chain networks

Figure 16 shows the axial force of the strong force chains in Figures 14 and 15 in the case of $p' = 50$ and 200 kPa and $i = 2.0$. For samples with $F_c = 35\%$ (ie, fines overfilled the voids between coarse grains), the axial force gradually increased before the turning point, implying that the external force was transferred to the strong force chain. At the turning point, the axial force reached its maximum value and then decreased to a minor value. For samples with $F_c = 20\%$ (ie, fines underfilled the voids between coarse grains), Figure 16A shows that the axial force of the strong force chain was unchanged during the suffusion process. The decrease in the contact force between particles thus made the particles more vulnerable to detach.[53,15,29] Figure 16B shows the angle magnitude of the strong force chain in Figures 14 and 15. The angle magnitude ($\theta$) is illustrated in the inset of Figure 16B. It is defined as the angle (in degree) between two vectors that point from the center of a particle (particle 2, see inset of Figure 16B) to that of its two neighboring particles (particles 1 and 3, see inset of Figure 16B) in a force chain. The apparent decrease in the strong force chain angle for samples with $F_c = 35\%$ (ie, fines overfilled the voids between coarse grains) indicated that the force chain buckled at the turning point in these cases. For samples with $F_c = 20\%$ (ie, fines underfilled the voids between coarse grains), the force chain angle was constant during suffusion, which was in accordance with behavior of the local specimen profile, as shown in Figure 15.

Figure 17 shows the evolution of the ratio of the average contact force to the fluid force ($F_{cont}/F_{fluid}$) for the fine particles in a local packing of the sample with $F_c = 35\%$ under $p' = 50$ kPa. The average contact forces for the fine particles in the local packing are two to six times the fluid forces applied to them at the initiation of suffusion. It is observed that several
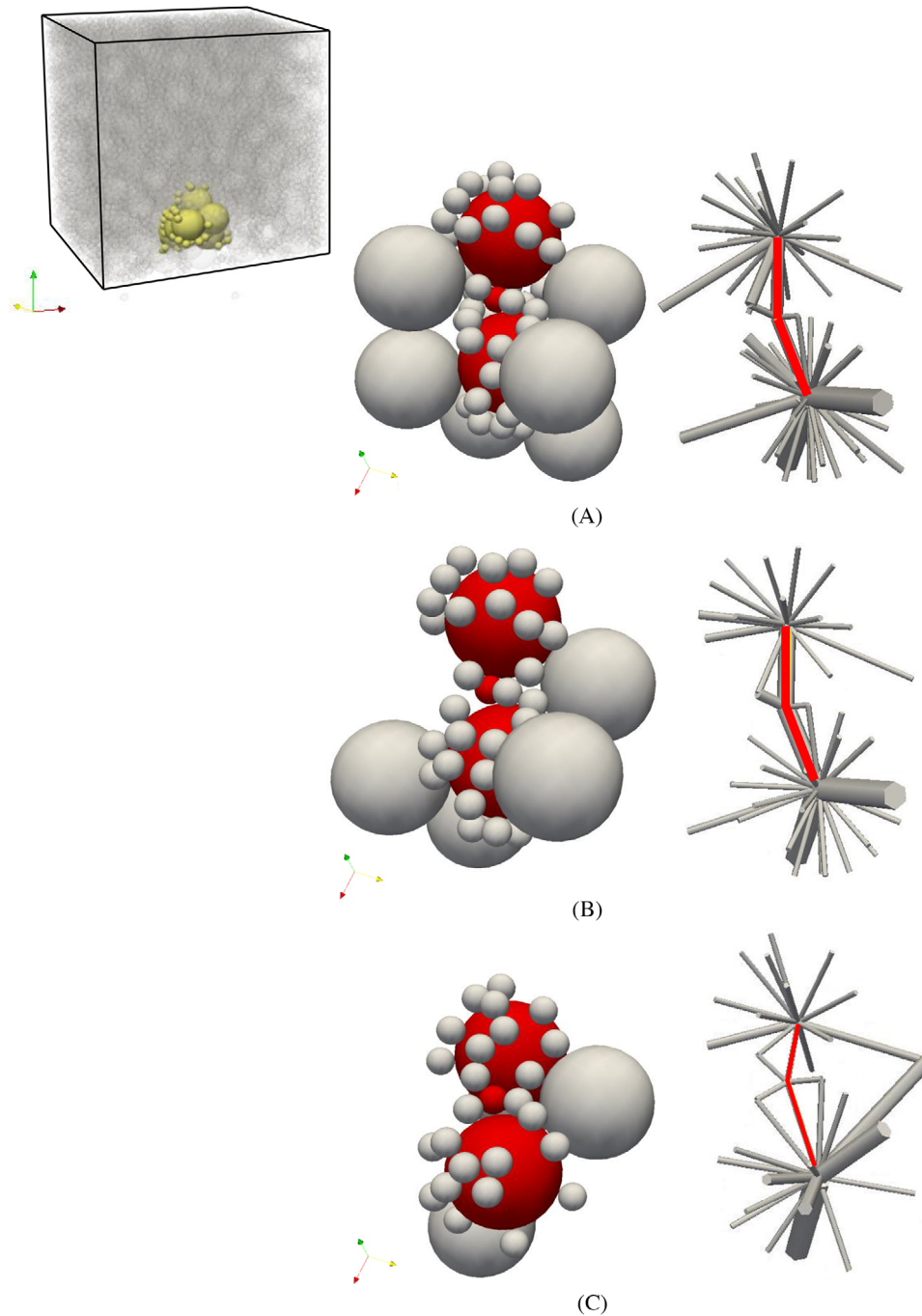
**FIGURE 14** The evolution of local packings during erosion for samples with $F_c = 35\%$: (A) initial configuration and (B) before turning point, and (C) after turning point

fine particles with a low $F_{cont}/F_{fluid}$ are first detached from the chained particles at about 2.1 seconds. The ratios of the average contact forces to the fluid forces for these fine particles continue to decrease before being eroded. These fine particles around chained particles involve in the force chain and provide more important lateral support. When a certain amount of the fine particles providing the lateral support is lost, the buckling of the chained particles occurs, as shown in the inset of Figures 17 and 14. Subsequently, more fine particles supported by the chained particles are released and eroded at 3.6 seconds, as shown in the inset of Figure 17. The $F_{cont}/F_{fluid}$ for some remaining fine particles increases obviously due to the stress transfer during the rearrangement of the particles.

Previous analyses show that strong force chain buckling weakened the contact forces on fine particles[54,55,52] and then facilitate the erosion of these fine particles. To explain the different effects of $p'$ on the cumulative fines loss, Figures 7, 8,
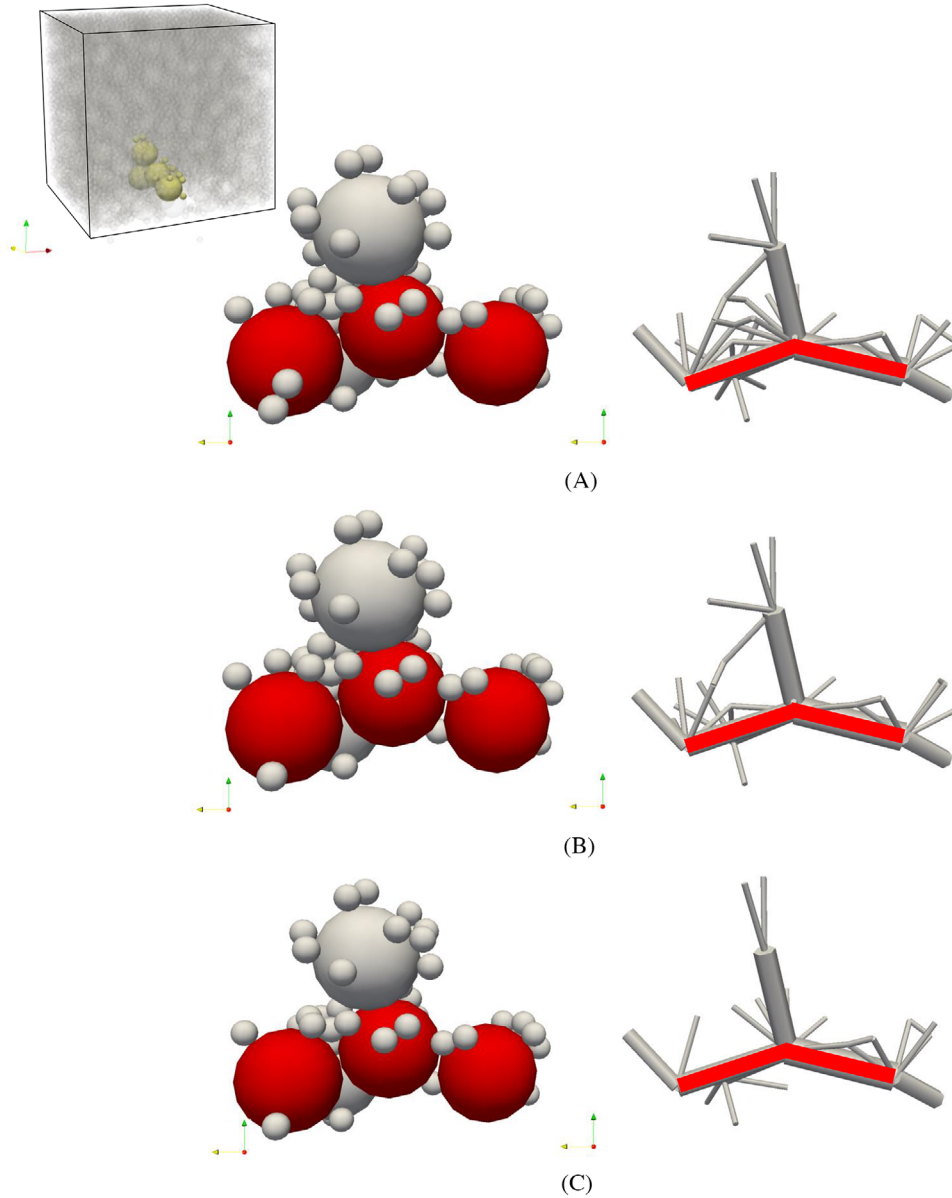
**FIGURE 15** The evolution of local packings during erosion for samples with $F_c = 20\%$: (A) initial configuration, (B) before turning point, and (C) after turning point

and 18 show the percentage by quantity of buckled strong force chains during suffusion for the samples with $F_c = 20\%$ and 35% under $p' = 50$ and 200 kPa. Figure 18 shows that the percentage by quantity of the buckled strong force chains increased dramatically at the turning point for samples with $F_c = 35\%$ (ie, fines overfilled the voids between coarse grains) under $p' = 50$ and 200 kPa. After the sudden increase of the buckling fraction, the eroded particles mass also increased as shown in Figure 7. Further inspection into the computed results reveals that the erosion intensification following force chain buckling is linked to the release of new free particles. For the sample with higher confining pressure ($p' = 200$ kPa), the buckling fraction was larger, resulting in a larger eroded particles mass under this condition. As the discharge of eroded fine particles stabilized, the buckling fraction degraded gradually for the samples with $F_c = 35\%$ under both confining pressures. Due to the short simulation time, the sample was hardly stable when subjected to seepage flow, resulting in the existence of an appreciable buckling fraction at the final stage. While for the samples with $F_c = 20\%$ (ie, fines underfilled the voids between coarse grains), under both confining pressures, the fraction of buckled strong force chains remained small and constant during suffusion, meaning that the original load-bearing skeleton was stable.
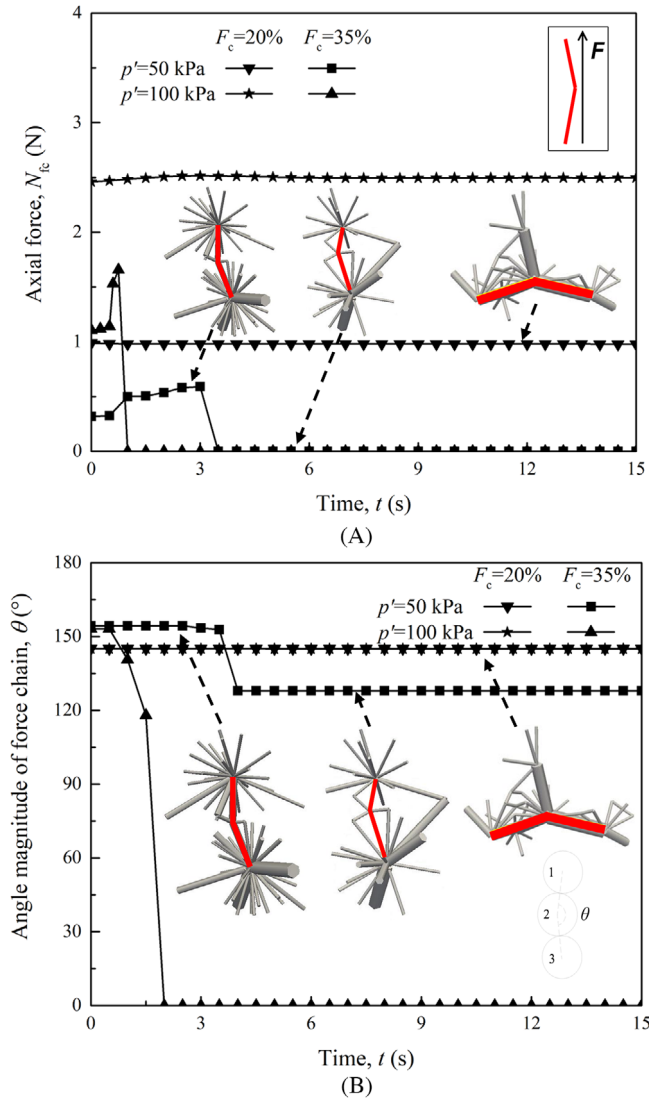
**FIGURE 16** Evolution of (A) axial force and (B) angle magnitude for a typical force chain in samples with different $F_c$ (20% and 35%) and $p'$ (50 and 200 kPa) (angle of 0° means that the contact is separated)

## 5.4 | Energy evolution during suffusion

The strong force chain buckling and induced collapse of the strong network caused the strain energy stored in the contacts to be released, especially the strain energy within strong fine-fine contacts.

Figure 19 shows the evolution of the strain energy within strong fine-fine contacts during suffusion for samples with $F_c$ = 20% and 35% under $p'$ = 50 and 200 kPa. At the turning point, the strain energy within strong fine-fine contacts started to decrease for samples with $F_c$ = 35% (ie, fines overfilled the voids between coarse grains) under both confining pressures. It was noted that the strain energy in the sample with higher confining pressure ($p'$ = 200 kPa) experienced the greatest decrease due to strongest contact forces acting on the fines. For samples with $F_c$ = 20% (ie, fines underfilled the voids between coarse grains), the strain energy within strong fine-fine contacts was almost not released during suffusion. This was because the external force was primarily transmitted by coarse particles for this sample, as show in Figure 15. The strain energy within fine-fine contacts was relatively lower than that of the sample with $F_c$ = 35% (ie, fines overfilled the voids between coarse grains) due to the small magnitude of fine-fine contact forces.

The release of strain energy due to the collapse of the strong network will accelerate particle movement. Figure 20 shows the kinetic energy of fine and coarse particles in samples with different fines contents and confining pressures. The kinetic energy of a particle in this study is the summation of its translational and rotational kinetic energies that are,
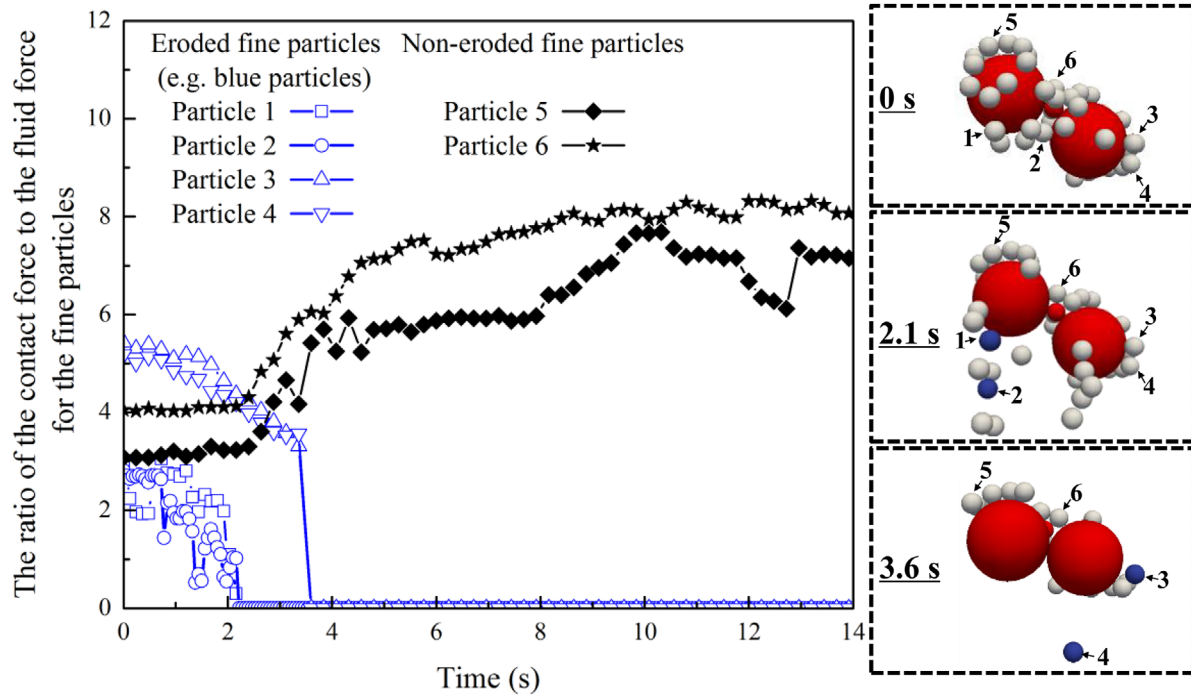
**FIGURE 17** Evolution of the ratio of the average contact force to the fluid force for the fine particles in a local packing ($F_c = 35\%$, $p' = 50$ kPa)
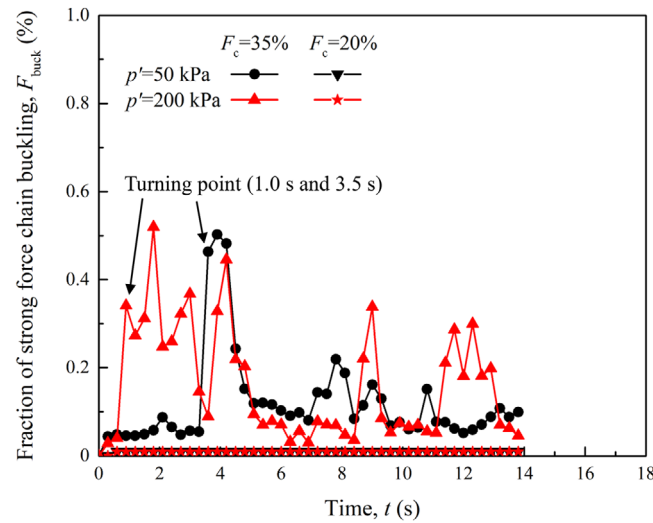


**FIGURE 18** Fraction of strong force chain buckling for the samples with different $F_c$ (20% and 35%) and $p'$ (50 and 200 kPa)

respectively, calculated as[43,64]

$$E_{kt} = \frac{1}{2} \sum_{i=1}^{N_p} m_i v_i^2 \tag{20}$$

$$E_{kr} = \frac{1}{2} \sum_{i=1}^{N_p} I_i \omega_i^2, \tag{21}$$

where $m_i$ is the mass of particle $i$. $v_i$ and $\omega_i$ are the translational and rotational speeds of particle $i$, respectively. $N_p$ is the total number of fine particles. $I_i = 0.4 m_i r_i^2$ is the moment of inertia of particle $i$.
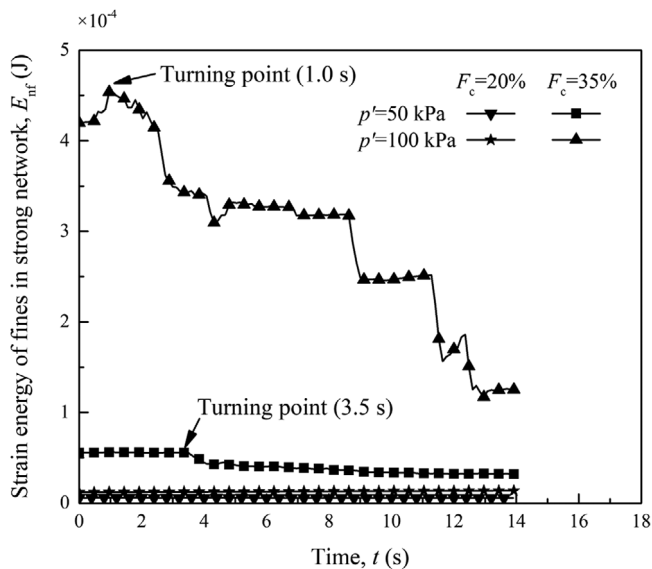
**FIGURE 19** Strain energy of fines in strong network for the samples with different $F_c$ (20% and 35%) and $p'$ (50 and 200 kPa)
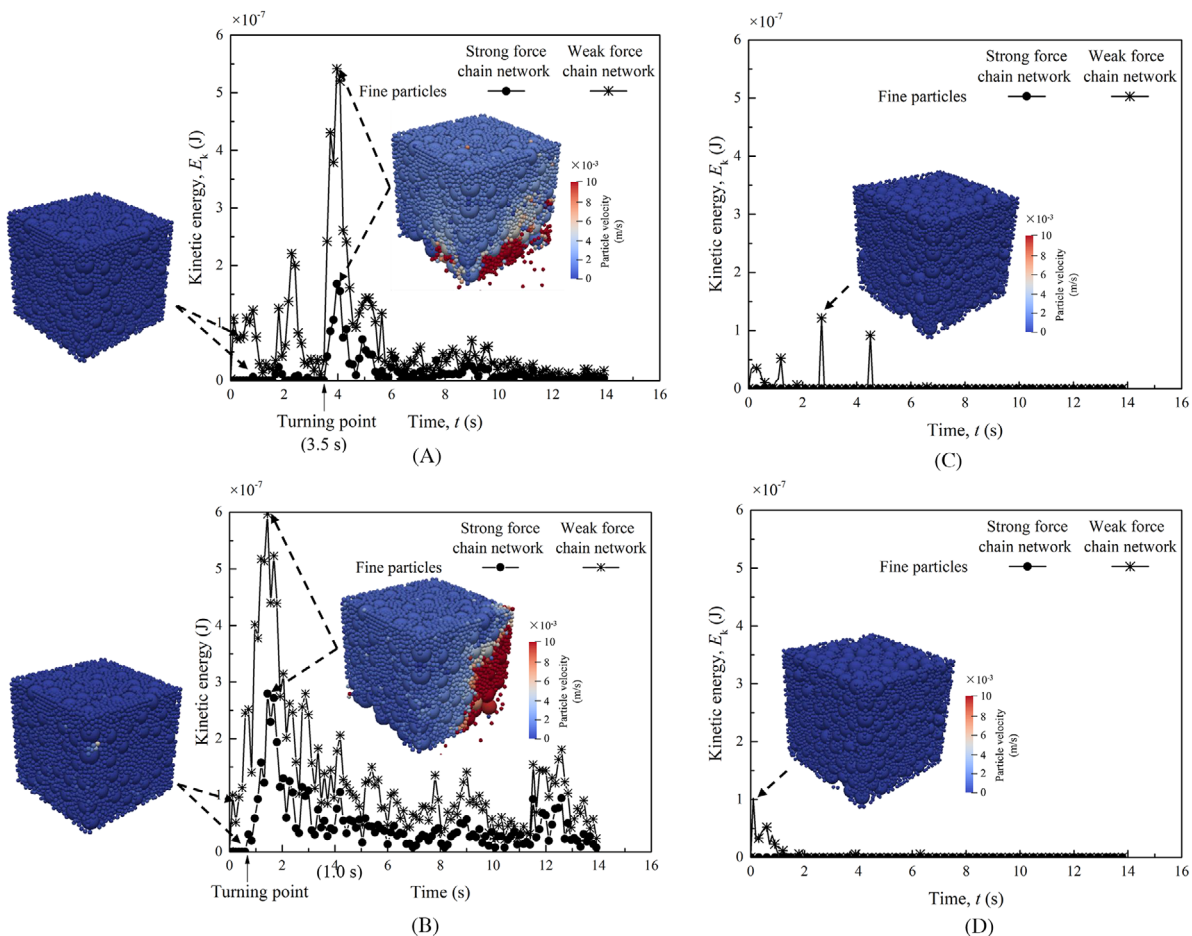


**FIGURE 20** Kinetic energy of the fine particles in different networks for the samples with (A) $F_c = 35\%$, $p' = 50$ kPa; (B) $F_c = 35\%$, $p' = 200$ kPa; (C) $F_c = 20\%$, $p' = 50$ kPa; and (D) $F_c = 20\%$, $p' = 200$ kPa
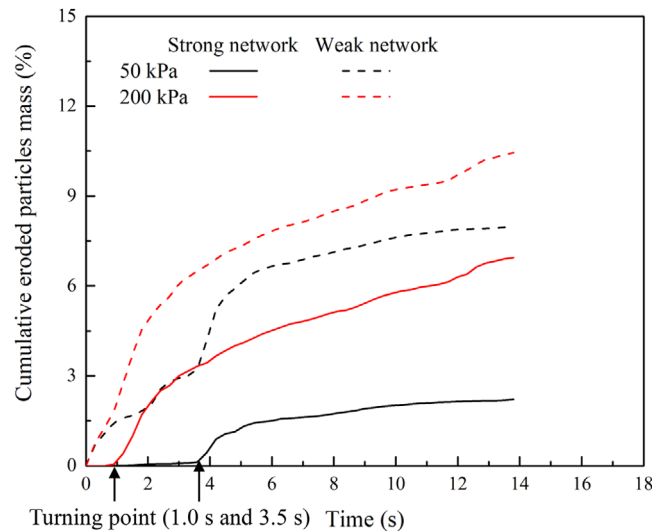
**FIGURE 21** Cumulative eroded mass of fines in strong and weak networks for Fc=35%

For the samples with $F_c = 35\%$ (ie, fines overfilled the voids between coarse grains), the kinetic energy of both kinds of particles increased dramatically after the turning point due to strong force chain buckling,[54,55,52] which intensified suffusion. In contrast, before the turning point, only particles in the weak network had high kinetic energy because in this phase, the strong network of the sample was relatively stable and only fines with low connectivity and contact forces were eroded. Figures 20A and B also show that kinetic energy of the particles in the sample under higher confining pressure was higher than that under lower confining pressure, which is consistent with the extent of the released strain energy for the respective samples. Figures 20C and D show that the kinetic energy of fines in the sample with $F_c = 20\%$ (ie, fines underfilled the voids between coarse grains) was much lower than that of the sample with $F_c = 35\%$ (ie, fines overfilled the voids between coarse grains) due to lower released strain energy of fines.

Figure 21 shows the cumulative eroded mass of fines in the strong and weak networks for the samples with $F_c = 35\%$ (ie, fines overfilled the voids between coarse grains) under $p' = 50$ and 200 kPa. It is obvious that after the turning point, the fines in the strong network (the fine particles with contact forces of which the magnitude is larger than the average contact forces) started to be eroded, which is consistent with the variation of the kinetic energy of strong network before and after the turning point. The mechanical instability of gap-graded soil subjected to suffusion, as discussed above, is interpreted in the context of evolving kinematic and strain energies. This instability problem should be further analyzed using the second-order work criterion, which remains to be the authors' future pursuit.

# 6 | CONCLUSIONS AND DISCUSSION

This study presents a coupled CFD-DEM investigation, with the aim to understand the coupling effect of $p'$ and $F_c$ on the erodibility of gap-graded coarse-grained soil, and to shed micromechanical insights into the phenomenon. Typical ranges of $F_c$ (20% to 35%) and $p'$ (50 to 200 kPa) are considered. The simulated results of eroded particles mass and samples deformation were presented and interpreted from a micromechanical perspective, including the evolution of force transmission structure, force chain buckling, and strain energy release under the action of suffusion.

It is revealed from the coupled CFD-DEM investigation that when the fines overfilled the voids between coarse particles (ie, $F_c > 25\%$) and participated heavily in load-bearing, the erosion of the fines (triggered by a hydraulic gradient $i = 2$ in this study) could lead to the buckling of the strong force chains, and cause a significant collapse of the original force transmission structure. The sudden collapse has facilitated particle movement and strain energy release, which intensified suffusion. The aforementioned observations become more pronounced for a higher confining stress $p'$.

On the contrary, for the samples with the fines underfilled the voids between coarse particles (ie, $F_c < 25\%$), only fines that do not fill the voids were eroded that had little influence on the force network. High confining pressure in this case increased the contact forces between fines, which may had served as a stabilizer to maintain the contact structure and prevent the occurrence of suffusion.

The notion of active fine fraction could be used to understand the consequences of suffusion for large $F_c$. The concept of preferential growth of contact forces[56] can help understand the poor influence of $p'$ on the eroded mass observed in this study. Indeed, if contact forces increase as a fraction of their current value under an increase in $p'$, the weak contact force does not increase much in absolute value[56] and remain small enough with respect to fluid forces. The definition of force chain as well as buckling of force chains is introduced but the influence of the topology of the surrounding weak phase could be investigated more deeply as it is known to control force chain stability.[57] For large $F_c$, fine particles are probably more involved in force chains[58] and in the same time, the weak phase provides a more important lateral support.[59] Under such hypothesis, an erosion of some fine particles will lead to more dramatic consequences.

**DATA AVAILABILITY STATEMENT**

The numerical data used to support the findings of this study (NAG3151) are available from the corresponding author upon request.

**ORCID**

*Yi Hong* https://orcid.org/0000-0002-5984-8204
*Jidong Zhao* https://orcid.org/0000-0002-6344-638X

**REFERENCES**

1. Tomlinson SS, Vaid YP. Seepage forces and confining pressure effects on piping erosion. *Can Geotech J*. 2000;37:1-13.
2. Papamichos E, Vardoulakis I, Tronvoll J, Skjvrstein A. Volumetric sand production model and experiment. *Int J Numer Anal Meth Geomech*. 2001;25:789-808.
3. Bendahmane F, Marot D, Alexis A. Experimental parametric study of suffusion and backward erosion. *J Geotech Geoenviron Eng*. 2008;134:57-67.
4. Richards KS, Reddy KR. True triaxial piping test apparatus for evaluation of piping potential in earth structures. *J ASTM Geotech Test*. 2010;33(1):83-95.
5. Li M, Fannin RJ. A theoretical envelope for internal instability of cohesionless soil. *Géotechnique*. 2012;62(1):77-80.
6. Luo YL, Jin X, Li X, Zhan ML, Sheng JC. A new apparatus for evaluation of contact erosion at the soil-structure interface. *Geotech Test J*. 2013;36:256-263.
7. Chang DS, Zhang LM. Critical hydraulic gradients of internal erosion under complex stress states. *J Geotech Geoenviron Eng*. 2013;139(9):1454-1467.
8. Shire T, O'Sullivan C. Micromechanical assessment of an internal stability criterion. *Acta Geotech*. 2013;8:81-90.
9. Shire T, O'Sullivan C, Hanley KJ, Fannin RJ. Fabric and effective stress distribution in internally unstable soils. *J Geotech Geoenviron Eng*. 2014;140(12):04014072.
10. Ke L, Takahashi A. Experimental investigations on suffusion characteristics and its mechanical consequences on saturated cohesionless soil. *Soils Foundations*. 2014;54(4):713-730.
11. Wang S, Chen JS, Luo YL, Sheng JC. Experiments on internal erosion in sandy gravel foundations containing a suspended cutoff wall under complex stress states. *Nat Hazards*. 2014;74:1163-1178.
12. Liang Y, Yeh TCJ, Wang JJ, Liu MW, Zha YY, Hao YH. Onset of suffusion in upward seepage under isotropic and anisotropic stress conditions. *Eur J Environ Civil Eng*. 2019;23:1520-1534.
13. Yang J, Yin Z-Y, Laouafa F, Hicher P-Y. Internal erosion in dike-on-foundation modeled by a coupled hydro-mechanical approach. *Int J Numer Anal Methods Geomech*. 2019;43(3):663-683.
14. Yang J, Yin Z-Y, Laouafa F, Hicher P-Y. Three-dimensional hydro-mechanical modelling of internal erosion in dike-on-foundation. *Int J Numer Anal Methods Geomech*. 2020;44(8):1200-1218.
15. Kawano K, Shire T, O'Sullivan C. Coupled particle-fluid simulations of the initiation of suffusion. *Soils Foundations*. 2018;58(4):972-985.
16. Hu Z, Zhang YD, Yang ZX. Suffusion-induced deformation and microstructural change of granular soils: a coupled CFD-DEM study. *Acta Geotech*. 2019;14(3):795-814.
17. Xiong H, Yin Z-Y, Zhao J, Yang Y. Investigating the effect of flow direction on suffusion and its impacts on gap-graded granular soils. *Acta Geotech*. 2020. https://doi.org/10.1007/s11440-020-01012-9.
18. Jin T, Luo K, Fan J, Yang J. Immersed boundary method for simulations of erosion on staggered tube bank by coal ash particles. *Powder Technol*. 2012;225:196-205.

19. Wang M, Feng YT, Pande GN, Chan AHC, Zuo WX. Numerical modelling of fluid-induced soil erosion in granular filters using a coupled bonded particle lattice Boltzmann method. *Comput Geotech*. 2017;82:134-143.

20. Wang M, Feng YT, Owen DRJ, Qu TM. A novel algorithm of immersed moving boundary scheme for fluid–particle interactions in DEM–LBM. *Comput Meth Appl Mech Eng*. 2019;346:109-125.

21. Luo YL, Luo B, Xiao M. Effect of deviator stress on the initiation of suffusion. *Acta Geotech*. 2019;15:1607-1617.

22. Wautier A, Bonelli S, Nicot F. DEM investigations of internal erosion: grain transport in the light of micromechanics. *Int J Numer Anal Meth Geomech*. 2019;43:339-352.

23. Israr J, Indraratna B. Study of critical hydraulic gradients for seepage-induced failures in granular soils. *J Geotech Geoenviron Eng*. 2019;145(7):04019025.

24. Goniva C, Kloss C, Deen NG, et al. Influence of rolling friction on single spout fluidized bed simulation. *Particuology*. 2012;10:582-591.

25. Kloss C, Goniva C, Hager A, Amberger S, Pirker S. Models, algorithms and validation for opensource DEM and CFDDEM. *Progr Comput Fluid Dyn*. 2012;12(2-3):140-152.

26. Mindlin RD, Deresiewicz H. Elastic spheres in contact under varying oblique forces. *Trans ASME Ser E J Appl Mech*. 1953;20:327-344.

27. Renzo AD, Maio FPD. Comparison of contact-force models for the simulation of collisions in DEM-based granular flow codes. *Chem Eng Sci*. 2004;59(3):525-541.

28. Zhu HP, Zhou ZY, Yang RY, Yu AB. Discrete particle simulation of particulate systems: theoretical developments. *Chem Eng Sci*. 2007;62:3378-3396.

29. Hosn RA, Sibillea L, Benahmedb N, Chareyre B. A discrete numerical model involving partial fluid-solid coupling to describe suffusion effects in soils. *Comput Geotech*. 2018;95:30-39.

30. Di Felice R. The voidage function for fluid-particle interaction systems. *Intl J Multiphase Flow*. 1994;20:153-159.

31. Zhou ZY, Kuang SB, Chu KW, Yu AB. Discrete particle simulation of particle-fluid flow: model formulations and their applicability. *J Fluid Mech*. 2010;661:482-510.

32. Anderson TB, Jackson R. Fluid mechanical description of fluidized beds. Equations of motion. *Ind Eng Chem Fundam*. 1967;6:527-539.

33. Concha F. Settling velocities of particulate systems. *KONA Powder Particle J*. 2009;27:18-37.

34. Zhao J, Shan T. Coupled CFD-DEM simulation of fluid-particle interaction in geomechanics. *Powder Technol*. 2013;239:248-258.

35. Suzuki K, Bardet JP, Oda M, et al. Simulation of upward seepage flow in a single column of spheres using discrete-element method with fluid-particle interaction. *J Geotech Geoenviron Eng*. 2007;133(1):104-109.

36. Ergun S. Fluid flow through packed columns. *Chem Eng Prog*. 1952;48(2):89-94.

37. Kezdi A. *Soil Physics-Selected Topics*. Amsterdam: Elsevier Scientific Publishing Co.; 1979.

38. Kenney TC, Lau D. Internal stability of granular filters. *Can Geotech J*. 1985;22(2):215-225.

39. Widuliński L, Kozicki J, Tejchman J. Numerical simulations of triaxial test with sand using DEM. *Arch Hydro-Eng Environ Mech*. 2009;56(3-4):149-171.

40. Cundall PA, Strack ODL. A discrete numerical model for granular assemblies. *Geotechnique*. 1979;29(1):47-65.

41. Salot C, Gotteland P, Villard P. Influence of relative density on granular materials behavior: dEM simulations of triaxial tests. *Granular Matter*. 2009;11:221-236.

42. Chang CS, Meidani M. Dominant grains network and behavior of sand-silt mixtures: stress-strain modeling. *Int J Numer Anal Methods Geomech*. 2013;37(15):2563-2589.

43. Hanley KJ, Huang X, O'Sullivan C. Energy dissipation in soil samples during drained triaxial shearing. *Géotechnique*. 2018;68(5):421-433.

44. Ke L, Takahashi A. Drained monotonic responses of suffusional cohesionless soils. *J Geotech Geoenviron Eng*. 2015;141:04015033.

45. Minh NH, Cheng YP, Thornton C. Strong force networks in granular mixtures. *Granular Matter*. 2014;16:69-78.

46. Wu C, Chu J. Biogrouting method for stronger bond strength for aggregates. *J Geotech Geoenviron Eng*. 2019;146:06020021.

47. Wu C, Chu J, Wu S, Cheng L, von Paassen L. Microbially induced calcite precipitation along a circular flow channel under a constant flow condition. *Acta Geotech*. 2019;14(3):673-683.

48. Radjai F, Wolf D, Jean M, Moreau JJ. Bimodal character of stress transmission in granular packings. *Phys Rev Lett*. 1998;80:61-64.

49. Thornton C, Antony SJ. Quasi-static deformation of particulate media. *Philos Trans R Soc A*. 1998;356:2763-2782.

50. Tordesillas A, Zhang J, Behringer R. Buckling force chains in dense granular assemblies: physical and numerical experiments. *Geomech Geoeng*. 2009;4:3-16.

51. Tordesillas A, Steer C, Walker D. Force chain and contact cycle evolution in a dense granular material under shallow penetration. *Nonlinear Processes Geophys*. 2014;21:505-519.

52. Nicot F, ·Xiong H, Wautier A, Lerbet J, Darve F. Force chain collapse as grain column buckling in granular materials. *Granular Matter*. 2017;19(1-12):18.

53. Zhang F, Li ML, Peng M, Chen C, Zhang LM. Three-dimensional DEM modeling of the stress-strain behavior for the gap-graded soils subjected to internal erosion. *Acta Geotech*. 2018;14(66):1-17.

54. Bi ZW, Sun QC, Jin F, Zhang M. Numerical study on energy transformation in granular matter under biaxial compression. *Granular Matter*. 2011;13:503-510.

55. Nguyen HNG, Prunier F, Djéran-Maigre I, Nicot F. Kinetic energy and collapse of granular materials. *Granular Matter*. 2016;18:1-10.

56. Pouragha M, Duriez J, Wautier A, Wan R, Nicot F, Darve F. Preferential growth of force network in granular media. *Granular Matter*. 2019;21:67.

57. Tordesillas A, Lin Q, Zhang J, Behringer RP, Shi J. Structural stability and jamming of self-organized cluster conformations in dense granular materials. *J Mech Phys Solids*. 2011;59:265-296.

58. Shire T, O'Sullivan C, Hanley KJ. The influence of fines content and size-ratio on the micro-scale properties of dense bimodal materials. *Granular Matter*. 2016;18:52.

59. Wautier A, Bonelli S, Nicot F. Flow impact on granular force chains and induced instability. *Phys Rev E*. 2018;98:042909.

60. Chang DS. *Internal Erosion and Overtopping Erosion of Earth Dams and Landslide Dams* (PhD thesis). Hong Kong University of Science and Technology; 2012.

61. Israr J, Indraratna B. Internal stability of granular filters under static and cyclic loading. *J Geotech Geoenviron Eng*. 2017;143(6):04017012.

62. Kloss C, Goniva C, Hager A, et al. Models, algorithms and validation for opensource DEM and CFD-DEM. *Prog Comput Fluid Dyn Int J*. 2012;12:140-152.

63. Nguyen CD, Benahmed N, Ando E, Sibille L, Philippe P. Experimental investigation of microstructural changes in soils eroded by suffusion using X-ray tomography. *Acta Geotech*. 2019;14:749-765.

64. Wang P, Arson C. Energy distribution during the quasi-static confined comminution of granular materials. *Acta Geotechnica*. 2018;13 1075–1083.

65. Hu Zheng, Zhang Yida, Yang Zhongxuan. Suffusion-induced deformation and microstructural change of granular soils: a coupled CFD–DEM study. *Acta Geotechnica*. 2019;14 (3):795–814. https://doi.org/10.1007/s11440-019-00789-8.